Article:
Iaconis, P., Lagostina, V., Ricco, F. et al. (2026) MXenes as electron mediators in photocatalysis: Structural advantages and integration into advanced heterojunctions. International Journal of Hydrogen Energy, 238. 155192. ISSN: 0360-3199

https://doi.org/10.1016/j.ijhydene.2026.155192

International Journal of Hydrogen Energy 238 (2026) 155192

Contents lists available at ScienceDirect

International Journal of Hydrogen Energy

journal homepage: www.elsevier.com/locate/he

MXenes as electron mediators in photocatalysis: Structural advantages and integration into advanced heterojunctions

Paolo Iaconis [b], Valeria Lagostina [a], Francesco Ricco [a], Gabriele Enrico [a], Matthew J. Wigglesworth [c], Sergio Vernuccio [d], Paola Calza [a], Maria Cristina Paganini [a,*]

[a] Department of Chemistry, University of Turin, Via P. Giuria 5-7, 10125, Torino, Italy
[b] Department of Chemistry and Bioscience, Fredrik Bajers Vej 7H, room: 3.305, 9220, Aalborg Øst, Denmark
[c] School of Chemical, Materials and Biological Engineering, University of Sheffield, Sheffield, S1 3JD, United Kingdom
[d] School of Chemistry and Chemical Engineering, University of Southampton, Highfield Campus, Southampton, SO17 1BJ, United Kingdom

ARTICLE INFO

Keywords:
MXene heterojunction
Zinc oxide
Zinc oxide/cerium oxide composite
hydrogen production

ABSTRACT

In this work, we investigate MXene-based heterojunctions engineered to improve photocatalytic performance by promoting interfacial charge transfer and suppressing electron–hole recombination. The coupling of Ti_3C_2 MXene with ZnO is explored as a strategy to obtain more favourable band alignment. Multiple synthesis routes are employed, followed by comprehensive structural, morphological, and electronic characterization. Complementary Density Functional Theory (DFT) calculations are proposed to elucidate reaction barriers for water oxidation and hydrogen adsorption, providing theoretical insight into the observed catalytic behaviour. Overall, this study aims to advance the development of MXene-based heterojunction photocatalysts for sustainable hydrogen production and broader solar-driven applications. The ternary mixed systems were synthesized using two different methods, highlighting the key role of the preparation route in determining the structural properties and photocatalytic performance of the materials. Results obtained in hydrogen production, even preliminary, are encouraging especially for the ternary system MXene with zinc oxide coupled with cerium oxide.

1. Introduction

Fossil fuels still represent the global primary energy source. However, in recent decades, increasing awareness of their negative impact on environmental and atmospheric pollution has driven governments, international organizations, institutions, and industries to collaborate and invest in the development of alternative energy sources. The overarching goal is to reduce dependence on non-renewable resources and promote the long-term sustainable development of human society [1].

Among these alternatives, solar energy stands out as one of the most promising resources for addressing current energy and environmental challenges, being both abundant and clean. Nevertheless, its efficient conversion into useable forms of energy requires advanced materials capable of capturing and transforming solar radiation into chemical energy.

In this context, photocatalysis has gained substantial attention, especially in recent years, as a key technology for the direct utilization of solar energy. It offers a promising pathway to produce sustainable fuels such as hydrogen, as well as for the degradation of harmful pollutants and the reduction of CO_2 [2].

Despite significant progress since the pioneering work of Honda and Fujishima in 1972 [3], the overall efficiency of photocatalytic materials remains a major limitation to their widespread application. The efficiency of a photocatalytic system depends critically on several interconnected steps, and the optimization of each is essential for enhancing overall performance and achieving a more effective use of solar energy.

To overcome the limitations of traditional photocatalysts, research has increasingly focused on developing new materials and architectures capable of improving the separation and transfer of photogenerated charge carriers.

Over the past decade, MXenes have emerged as a versatile class of 2D materials with properties that distinguish them from conventional photocatalyst supports. Rather than acting merely as conductive additives, MXenes can influence multiple aspects of a photocatalytic system due to their layered morphology, metallic-like behaviour, and adjustable surface chemistry. Their stacked architecture enables intimate interfacial contact with semiconductors, while the presence of surface terminations can modulate electronic interactions and adsorption

* Corresponding author.
E-mail address: mariacristina.paganini@unito.it (M.C. Paganini).

https://doi.org/10.1016/j.ijhydene.2026.155192
Received 18 February 2026; Received in revised form 3 April 2026; Accepted 21 April 2026
Available online 5 May 2026

phenomena. While functioning as electron reservoirs, MXenes also can reshape charge-transfer pathways by modifying local electronic environments at the heterojunction interface. These combined effects make them particularly valuable for designing next-generation photocatalysts with enhanced light matter interactions and more efficient utilization of photogenerated carriers [4].

Due to its outstanding chemical, physical, and photocatalytic properties, MXenes are considered highly interesting even when compared to other 2D materials and have been extensively explored in various photocatalytic applications, including hydrogen production via water splitting [5], CO_2 reduction [6], and pollutant degradation [7].

Among the various strategies to enhance photocatalytic performance, the engineering of heterojunctions has emerged as one of the most effective approaches for developing advanced photocatalysts. In this study, MXenes are not employed as primary light absorbers, but are strategically incorporated as multifunctional cocatalytic components that regulate interfacial charge transfer. MXenes acts as electron reservoirs, Schottky junction formers, and interfacial bridges, stronglyimproving hydrogen evolution rates when coupled with semiconductors such as ZnO, MOF-derived ZnO, g-C_3N_4, and hybrid heterostructures. The central novelty is the demonstration that Ti_3C_2 MXene replaces Pt-like cocatalysts by functioning as a highly conductive electron sink. Favourable Fermi level alignment between Ti_3C_2Tx and the wide-bandgap semiconductors (e.g., ZnO) promotes unidirectional electron transfer, suppressing electron-hole recombination and accelerating HER kinetics. Moreover, surface terminations (–O, –OH, –F) on Ti_3C_2Tx provide chemically active sites for proton adsorption, improving hydrogen evolution kinetics. This combined electronic and catalytic functionality differentiates MXenes from graphene-like materials, which are largely inert without defect engineering [8,9]. Coupling MXenes with semiconductors significantly enhances photocatalytic system efficiency. This is attributed to their high electrical conductivity and a lower Fermi level compared to many semiconductors, which promotes the transfer of photogenerated electrons from the semiconductor to the MXene, making it an excellent electron acceptor. Additionally, the Fermi level difference between the two materials induces the formation of a Schottky barrier, which prevents electron–hole recombination in the semiconductor. This effective separation prolongs charge carrier lifetimes, increasing their availability for photocatalytic reactions and improving overall efficiency. However, the choice of semiconductor partners is crucial to ensure optimal interfacial interactions, effective band alignment, and improved separation of photogenerated charge carriers.

Recent literature reveals a clear trend toward the development of MXene-based heterojunctions with non-oxide semiconductors, such as metal chalcogenides (e.g., CdS, $ZnIn_2S_4$, MoS_2) and other narrow-bandgap systems, because these materials provide superior visible-light absorption and higher initial hydrogen evolution rates when coupled with MXenes [8,9].

However, these non-oxide MXene heterojunctions often suffer from limited chemical and photochemical stability. Many chalcogenides and sulfide-based photocatalysts are prone to photo-corrosion, surface oxidation, and structural degradation under prolonged irradiation and aqueous reaction conditions. As highlighted in the reviewed studies, this instability can lead to gradual performance decay, loss of active sites, and reduced long-term efficiency, despite high short-term catalytic activity. More recent studies have demonstrated that MXene-based heterostructures can significantly enhance photocatalytic hydrogen production. For example, MXene/semiconductor systems such as $ZnWO_4/Ti_3C_2$ heterojunctions have been shown to improve charge separation through built-in electric fields and band alignment, leading to enhanced hydrogen evolution rates and reduced recombination losses [10]. Similarly, 2D/2D MXene/CdS systems exhibit improved photocatalytic performance due to intimate interfacial contact and efficient electron transfer, further enhanced by photothermal effects and full-spectrum light absorption [11].

However, most of these studies focus on binary heterojunctions, where MXene primarily acts as an electron sink or conductive bridge. While this approach improves charge separation, it does not fully address the need for dynamic charge storage and redistribution, which are critical for sustaining photocatalytic reactions.

To overcome these limitations, recent research has explored more complex multi-component heterostructures, where additional materials are introduced to modulate charge transfer pathways. In particular, CeO_2 has attracted attention due to its reversible Ce^{4+}/Ce^{3+} redox couple, which enables electron trapping and release. For instance, advanced systems such as $Cd_{0.3}Zn_{0.7}S@Ti_3C_2/Ag/CeO_2$ have demonstrated that CeO_2 can participate in engineered charge-transfer pathways (e.g., Z-scheme or Schottky-assisted systems), enhancing photocatalytic hydrogen evolution through multi-channel electron transfer [12].

In contrast, MXene/oxide-based systems (e.g., MXene–ZnO, MXene–TiO_2, or MOF-derived oxide composites) generally exhibit lower hydrogen evolution rates compared to non-oxide counterparts, mainly due to wider band gaps and weaker visible-light absorption [13]. Nevertheless, oxide semiconductors offer significantly higher chemical robustness, resistance to oxidation, and long-term operational stability. For this reason, despite their comparatively lower peak performance, MXene/oxide heterojunctions can represent a more reliable and practical choice for sustained hydrogen production and real-world applications, where durability and reproducibility are as critical as catalytic efficiency. For all these reasons, while MXene heterojunctions with non-oxide semiconductors currently dominate the field in terms of maximum reported H_2 evolution rates, their intrinsic instability means they are not always the optimal solution, and oxide-based MXene systems remain highly relevant for the development of stable, scalable, and application-oriented hydrogen production technologies [13].

Building on these considerations, the present work aims to explore the synthesis and characterization of MXene-based heterojunctions, with the objective of optimizing their photocatalytic properties [14]. Among the wide range of photocatalysts reported in the literature, ZnO was selected in this study because it is a chemically stable oxide, low-cost, relatively non-toxic, and easily synthesizable using scalable and well-established methods. In addition, ZnO can be engineered into a variety of nanostructures that are particularly well suited for intimate interfacial contact with MXenes, favoring efficient charge transfer and heterojunction formation. Although oxide-based systems generally exhibit lower photocatalytic activity compared to MXene heterojunctions with non-oxide semiconductors, their superior chemical robustness and long-term stability make them more attractive for practical applications. The choice of cerium oxide (CeO_2) as the third component of the heterojunction was motivated by the fact that some of the authors have extensive prior experience in the synthesis and characterization of ZnO/CeO_2 binary systems [15]. These materials have already been prepared, thoroughly investigated, and tested in our laboratories, where they showed encouraging photocatalytic and charge-transfer properties. Building on this consolidated expertise, the introduction of CeO_2 in the present MXene-based ternary system represents a rational and knowledge-driven extension aimed at improving charge separation while maintaining high structural stability. Among all possible semiconductors MXenes can form a Schottky junction with ZnO, facilitating electron transfer from ZnO's conduction band to Ti_3C_2. This synergistic interaction reduces electron–hole recombination, significantly enhancing photocatalytic efficiency. Multiple synthesis strategies were investigated and complemented by a wide range of characterization techniques, including X-ray diffraction (XRD), field emission scanning electron microscopy (FESEM), UV–Vis spectroscopy, and electron paramagnetic resonance (EPR). These analyses provided a comprehensive understanding of the correlations between morphology, structure, and electronic properties and the photocatalytic activity of the developed materials. Furthermore, Density Functional Theory (DFT) calculations were proposed to elucidate the reaction barriers of water

and sacrificial agent oxidation, as well as the thermodynamics of hydrogen adsorption on MXene, thereby supporting the experimental observations. The overarching goal of the work is to contribute to the development of innovative photocatalytic materials with potential applications in sustainable hydrogen production. In this context, the present work aims to go beyond the extensively studied binary MXene/ZnO systems by introducing CeO_2 as a third component to construct a ternary MXene/CeO_2/ZnO heterostructure and by systematically comparing two different synthesis routes (hydrothermal vs precipitation). The novelty of this study lies in the combined investigation of (i) the role of CeO_2 as a redox-active component, (ii) the influence of the preparation method on the structural preservation of MXene and on interfacial contact, and (iii) the resulting impact on photocatalytic hydrogen evolution.

In particular, CeO_2 is not introduced as a passive secondary oxide, but as an active component capable of participating in a reversible Ce^{4+}/Ce^{3+} redox cycle, acting as an electron buffer and enabling an additional charge-transfer pathway beyond the conventional MXene-mediated electron extraction. The combination of MXene and CeO_2 is therefore expected to promote a dual charge management mechanism, where MXene facilitates fast electron transport while CeO_2 provides temporary charge storage and suppresses recombination. Furthermore, this work highlights how the synthesis route influences not only morphology and crystallinity, but also the chemical state of the components and the quality of the heterojunction interface, as demonstrated by XRD, EPR, and XPS analyses. The hydrothermal method, in particular, is shown to favour the coexistence of Ce^{3+}/Ce^{4+} species and better MXene structural preservation, which are directly linked to enhanced photocatalytic performance. Finally, the combination of experimental techniques (EPR and XPS) with DFT calculations provides a coherent interpretation of the charge-transfer mechanism in the ternary system, allowing us to rationalize the role of each component in the photocatalytic process. To the best of our knowledge, this study represents one of the few systematic investigations addressing the interplay between MXene, CeO_2, and ZnO in a ternary heterostructure, together with the effect of synthesis method on both structure and photocatalytic behaviour.

2. Experimental section

2.1. Materials

The Ti_3AlC_2 MAX phase (90%) 312 - 910767 (Sigma-Aldrich, CAS: 196506-01-1), Zinc acetate dihydrate 011559 (Alfa Aesar™, CAS: 5970-45-6), ethanol 1.00971 (SAFC, CAS: 64-17-5), HF solution (40% - 100335 (Aldrich-Merck, CAS: 7664-39-3), NaOH pellets 30620-M (Sigma-Aldrich, CAS: 1310-73-2), $CeCl_37H_2O$ 202983 (Sigma-Aldrich, CAS: 18618-55-8), $Zn(NO_3)_26H_2O$ 99% - 96482 (Sigma-Aldrich, CAS: 10196-18-6)

2.2. Preparation of MXene

MXene was synthesized via HF etching. Briefly, 2.0 g of Ti_3AlC_2 powder was gradually added to 40 mL of a 10% HF solution, taking care to control the temperature due to the highly exothermic nature of the reaction. The resulting suspension was stirred continuously at 500 rpm for 24 h. After etching, the suspension was centrifuged at 3500 rpm for 5 min to remove the acidic supernatant. The solid residue was subsequently washed and centrifuged three times with deionized water. Following these steps, the material was further purified by vacuum filtration using 1 L of deionized water on a cellulose membrane. Finally, the product was dried overnight at 70 °C. The obtained Ti_3C_2 MXene displayed the characteristic black colour.

2.3. Preparation of ZnO_P and CeO_2_ZnO_P semiconductors

ZnO was synthesized via a precipitation method. First, 3.0 g of zinc acetate dihydrate was dissolved in 12.5 mL of ethanol by heating the solution to 55 °C under continuous stirring. In parallel, 1.5 g of NaOH was dissolved in 6.25 mL of ethanol. The NaOH solution was then added dropwise to the zinc acetate solution, after which the resulting suspension was left undisturbed for 24 h at room temperature. At the end of the reaction, the supernatant was removed using a pipette. To purify the product, 20 mL of ethanol was added to the remaining solid, the mixture was stirred for 10 min, and then allowed to precipitate for 1 h. After precipitation, the supernatant was removed again. This washing–precipitation process was repeated three times.

Subsequently, the product underwent three centrifugation cycles at 5000 rpm for 10 min each, using ethanol as the washing medium. The resulting solid was filtered through a nylon membrane using ethanol and finally calcined at 300 °C for 4 h. The final product was labelled **ZnO_P**.

Similarly, the synthesis of CeO_2_ZnO materials followed the same procedure described above for ZnO_P. For the mixed samples, in addition to zinc acetate dihydrate ($Zn(CH_3COO)_2{\cdot}2H_2O$), 0.0376 g of cerium (III) chloride heptahydrate ($CeCl_3{\cdot}7H_2O$) corresponding to 1 mol% with respect to zinc acetate—was added to the initial solution. The final product was labelled **CeO_2_ZnO_P**.

2.4. Preparation of MXene_ZnO and MXene_CeO_2_ZnO heterojunctions

The MXene_ZnO heterojunction was prepared using two different methods: (i) a solid-state route in which precipitated ZnO was combined with MXene and subsequently calcined, and (ii) an in situ hydrothermal synthesis that directly produced the MXene_ZnO composite.

In the first method, 250 mg of MXene and 250 mg of ZnO_P were dispersed in 30 mL of deionized water. The suspension was magnetically stirred for 30 min, after which the solvent was evaporated in an oven at 70 °C for 18 h. The resulting dried solid was subsequently calcined in a muffle furnace at 450 °C for 4 h using a heating ramp of 5 °C min^{-1}. The final product was labelled **MXene_ZnO_P**. The same procedure was applied to the mixed systems CeO_2_ZnO, yielding the composite labelled **MXene_ CeO_2_ZnO_P.**

For the hydrothermal synthesis, 0.40 g of purified MXene was dispersed in 20 mL of deionized water and sonicated for 10 min to promote homogeneous dispersion and facilitate interlayer expansion. Subsequently, 5.95 g of zinc nitrate hexahydrate ($Zn(NO_3)_2{\cdot}6H_2O$) was dissolved into the mixture. The pH of the resulting solution was adjusted to 10–11 by the dropwise addition of 4 M NaOH. The suspension was then transferred to a PTFE-lined vessel sealed inside a 100 mL stainless-steel autoclave and heated at 175 °C for 12 h. After cooling to room temperature, the product was washed thoroughly with distilled water and subjected to three centrifugation cycles at 6000 rpm for 10 min each. The material was finally dried in an oven at 70 °C, yielding the sample labelled **MXene_6%_ZnO_H**.

Using the same hydrothermal method, two additional samples were prepared by adjusting the MXene content: 1 wt% MXene (0.060 g) and 12.6 wt% MXene (0.859 g), labelled **MXene_1%_ZnO_H** and **MXene_12%_ZnO_H**, respectively.

The synthesis of CeO_2 mixed MXene_6%_ZnO_H samples followed the same hydrothermal procedure. In this case, cerium(III) chloride heptahydrate ($CeCl_3{\cdot}7H_2O$, 0.0754 g) corresponding to 1 mol% relative to Zn $(NO_3)_2{\cdot}6H_2O$ was added to the precursor solution. The final product was labelled simply **MXene_ CeO_2_ZnO_H**.

2.5. Characterization

All the samples were analyzed via X-Ray Diffraction for the phase identification, moreover, the samples were studied using DR-UV-Visible spectroscopy, Field Emission SEM for the microstructure analysis, and a mass spectrometer was exploited to evaluate Hydrogen production.

In this work, the XRD analysis was performed utilizing a PANalytical PW3040/60 X'Pert PRO MPD diffractometer using a copper Kα radiation source (λ = 0.154056 nm). The UV-visible absorption spectra were

recorded using a Varian Cary 5000 spectrometer, coupled with an integration sphere for diffuse reflectance acquisition, using a Carywin-UV/scan software. A sample of PTFE with 100% reflectance was employed as the reference. Spectra were registered in the 200-2000 nm range at a scan rate of 240 nm/min with a step size of 1 nm. TESCAN, Bmo, Czech Republic was the SEM used for the microstructure study, it was coupled with Energy dispersive X-ray spectroscopy (EDS) (Oxford Ultim Max 100, Oxford Instruments, Abingdon, UK) for the creation of the element maps. Additionally, Field emission scanning electron microscopy (FESEM) was conducted using a TESCAN S9000G (Brno, Czech Republic) to examine the morphology of the MXene and heterojunctions particles. Imaging was performed using a working voltage of 10 keV. Elemental distribution of the samples was further investigated using energy-dispersive X-ray spectroscopy (EDX) coupled with FESEM. The electronic paramagnetic resonance measures were conducted with a CW-EPR EMX-Bruker spectrometer operating at X-band (9.5 GHz), equipped with a cylindrical cavity operating at 100 KHz field modulation and interfaced with a computer with WINEPR Acquisition program. The spectra have been recorded in a bath of liquid nitrogen (77 K). The specific surface area measurements were carried out on a Micromeritics ASAP 2020 using the Brunauer-Emmett-Teller (BET) model on the N_2 adsorption measurement. Prior to the adsorption run, all the samples were outgassed at 573 K for 2 h.

X-ray photoelectron spectroscopy (XPS) measurements were carried out using a PHI 5000 VersaProbe II (Physical Electronics, USA), equipped with a monochromatic Al Kα X-ray source (1486.6 eV). The X-ray beam was operated at a power of 24.78 W, and photoelectrons were collected at a take-off angle of 45° with respect to the sample surface. During the analyses, the pressure in the chamber was maintained below 10^{-5} Pa.

Survey spectra were acquired over a binding energy range from 0 to 1200 eV using a pass energy of 187.85 eV, while high-resolution spectra were recorded at a lower pass energy of 23.50 eV. To mitigate surface charging, a dual-beam neutralization system combining low-energy electrons and Ar^+ ions was employed. Energy calibration was performed by referencing the C 1s peak of titanium carbide at 281.9 eV for the pristine MXene sample, whereas for the other samples the C 1s signal at 284.8 eV (C–C/C–H) was used as an internal standard [16].

Data analysis and peak fitting were conducted using CasaXPS (version 2.3.18). A Shirley background was subtracted [17], and peak deconvolution was performed using mixed Gaussian–Lorentzian line shapes for oxide species, while asymmetric LA functions were adopted for carbide-related components. Quantitative elemental analysis was obtained from the integrated peak areas of the high-resolution spectra, applying the sensitivity factors supplied by the instrument manufacturer.

2.6. Photocatalytic hydrogen evolution

To assess the hydrogen generated during irradiation, a mass spectrometer was employed to analyse the gas emanating from the sample suspended in water solution. The reported hydrogen evolution rates were obtained from time-resolved measurements averaged over a stable steady-state regime; the associated uncertainties were calculated from the propagation of the calibration curve extrapolation error and the signal fluctuations in the steady-state region. For this set-up, 10 mg of photo-catalyst were weighted and suspended in a solution of 9 mL of distilled water and 1 mL of ethanol (used to increase the depletion of holes formed in the process). Ethanol was selected as sacrificial agent due to its lower toxicity and safer handling compared to methanol, while still providing effective hole scavenging). For the irradiation a UV lamp was used with a filter at a wavelength of 365 nm (THORSLAB, SOLIS-365C. 4W of power output).

Eventually, the effluent gas composition was monitored continuously with a Pfeiffer OmniSTAR GDS320 mass spectrometer connected to the cell outlet. Mass spectrometer data collection and visualization were performed via the QUADERA™ software from the same supplier. The duration of a typical experiment was 1 h.

2.7. Computational details

The computational methodologies have been described in detail in our previous work [18]. Comprehensive computational information specific to the ZnO and MXene systems is provided in the Supporting Information.

3. Results

3.1. Characterization techniques

In Fig. 1 the XRD patterns corresponding to MXene, MXene_ZnO_P and MXene_ZnO_H (with amount of MXene of 6% wt) mixed systems are reported. To improve clarity, the diffraction peaks are explicitly assigned in both the figure and the caption, where ZnO reflections are indicated by blue squares and MXene reflections by black spheres. The synthesis of MXene evidenced the presence of characteristic Ti_3C_2 peaks (Fig. 1a). The MXene phase was obtained by the exfoliation in a solution of 10% HF acid of the MAX phase obtaining the classic MXene structures recognized in the three main peaks at 9.2°, 18.7°, and 28.1° according to the literature data [19–21].

In Fig. 1a, the diffractograms of MXene_ZnO synthesized via hydrothermal and precipitation methods are shown alongside the pure MXene sample, allowing for a direct comparison among the three materials. Both MXene-ZnO samples display the typical diffraction peaks of ZnO, along with weak signals corresponding to MXene, confirming the coexistence of both phases. ZnO phase shows the typical pattern of a wurtzite hexagonal phase [15,22]. The diffraction peaks are relatively sharp suggesting the good crystallinity of the final product. In particular, the samples obtained via hydrothermal synthesis present a sharper signals indicating higher crystallinity and bigger crystals respect to the sample obtained via precipitation synthesis. Moreover, the peaks associated with the MXene phase are more evident in the sample obtained via hydrothermal synthesis compared to the one produced by precipitation. This difference can be attributed to variations in the structural preservation and dispersion of the MXene during the synthesis process. In particular, the hydrothermal route likely promotes a more controlled interaction between MXene and the oxide phases, favouring partial retention of its layered structure and a higher degree of ordering, which enhances the visibility of its characteristic diffraction peaks.

In contrast, the precipitation method may lead to a less homogeneous distribution of the MXene and a higher degree of structural disorder or restacking, as well as possible partial oxidation during synthesis and subsequent thermal treatment. These effects can reduce the intensity of the MXene-related reflections in the XRD patterns.

Therefore, the observed difference in peak intensity is interpreted as an indication of a higher relative preservation of the MXene structural features in the hydrothermally synthesized sample, although contributions from factors such as low loading, preferred orientation, and partial overlap with ZnO peaks should also be considered.

In addition, a diffraction peak observed at low angle ($2\theta \approx 7–8°$) is assigned to the (002) plane of Ti_3C_2Tx MXene, corresponding to the interlayer spacing of the layered structure. This peak is a characteristic feature of MXene materials and reflects the periodic stacking of Ti_3C_2 layers separated by surface terminations such as –O, –OH, and –F groups. The exact position and intensity of this reflection can be influenced by the degree of exfoliation, interlayer expansion, and possible structural modification during synthesis. To provide a more objective comparison of MXene retention, a semi-quantitative analysis was performed using the intensity ratio between the MXene (002) peak and the main ZnO (101) peak, I_{MXene}/I_{ZnO}. The results indicate that this ratio is higher in the hydrothermally synthesized sample compared to the precipitation-derived one, suggesting a greater relative preservation of

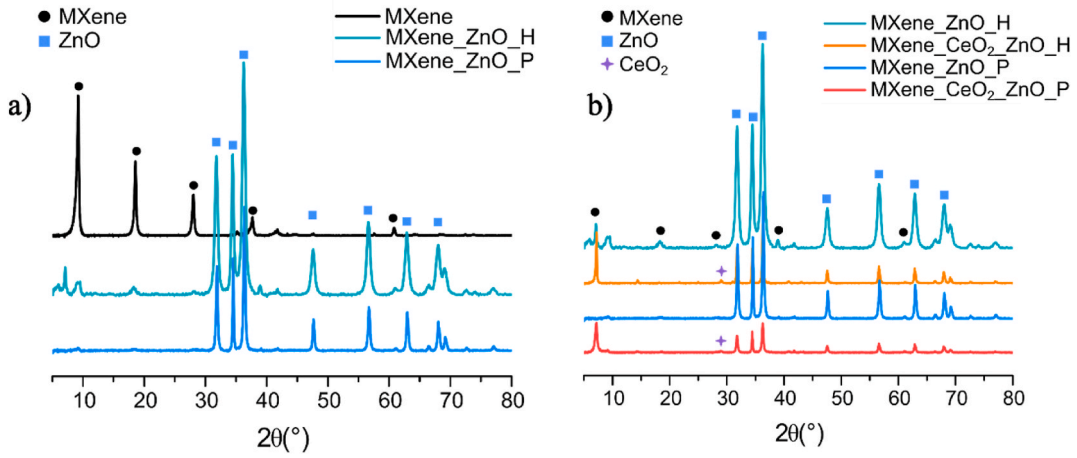

Fig. 1. XRD analysis of the tested samples, respectively: (a) Comparison between MXene and MXene_ZnO composite obtained via hydrothermal and precipitation way; (b) comparison among MXene_ZnO and MXene_CeO_2_ZnO composites obtained via hydrothermal and precipitation way. The MXene amount for all these sample is 6% in wt. The blue squares correspond to the standard peaks of wutzite ZnO structure and black balls to the MXene structure. The diffraction peaks corresponding to wurtzite ZnO are marked with **blue squares** and include the (100), (002), and (101) reflections (JCPDS No. 36-1451). The characteristic reflections of Ti_3C_2Tx MXene are indicated by **black spheres**, corresponding to the (002), (004), and (006) planes. The reference patterns for ZnO, CeO_2, and MXene are also included for comparison. The relative intensity of the MXene-related reflections is discussed in terms of structural retention and dispersion within the composite. (For interpretation of the references to colour in this figure legend, the reader is referred to the Web version of this article.)

the MXene structural features in the former. This difference may be attributed to a more favourable interaction between MXene and the oxide phases during hydrothermal synthesis, leading to reduced structural disorder or restacking. It should be noted that the I_{MXene}/I_{ZnO} ratio is used here as a comparative indicator within the same sample series and does not represent an absolute measure of crystallinity, as peak intensities in multiphase systems may also be influenced by preferred orientation, dispersion, and local structural disorder.

Furthermore, considering the calcination temperature (450 °C) for samples obtained through precipitation synthesis way, the relatively low intensity of MXene-related reflections may also reflect partial structural modification or oxidation of Ti_3C_2Tx, which is known to be sensitive to elevated temperatures. Nevertheless, the persistence of the MXene peak indicates that the layered structure is at least partially retained after synthesis.

In Fig. S1 samples obtained mixing different concentration of MXne and ZnO (respectively 1, 6, and 12 % of MXene) prepared via hydrothermal synthesis are presented. The sample with 6% in weight of MXene respect to ZnO seems to be the most interesting, cleaner and with both the components (MXene and ZnO) well visible, for this reason it has been selected for the preparation of the samples mixed with cerium oxide. Finally in Fig. 1b the diffraction peaks of pure ZnO prepared with Cerium oxide and coupled with MXene are presented. For the Ce-oxide composite, a faint additional peak at 28.9° appears, which can be attributed to CeO_2. According to our previous studies [12] Cerium ions (Ce^{4+} or Ce^{3+}) do not substitute Zn^{2+} within the ZnO lattice. Instead, they form nanosized CeO_2 domains that are deposited on the surface of ZnO crystals. This behaviour is likely due to the substantial mismatch in ionic radii between Ce^{4+}/Ce^{3+} and Zn^{2+}, as well as to the structural incompatibility between the cubic fluorite structure of CeO_2 and the wurtzite structure of ZnO. Aside from this slight variation, the coupling between CeO_2 and ZnO structure does not alter the overall XRD pattern relative to pure ZnO, as previously reported and demonstrated by some of us [15]. Again the different preparation ways lead to different crystallinity. Moreover the presence of Cerium oxide in the system further weakens the MXene signals, making them almost imperceptible in the samples obtained by the precipitation method. In the CeO_2 mixed sample synthesized hydrothermally, the MXene signal, although very weak, is still observable.

The specific surface area of the samples was determined by N_2 adsorption–desorption measurements, and the results are summarized in Table 1. All samples exhibit relatively low BET surface area values, ranging from 8 to 31 $m^2\,g^{-1}$. These values are consistent with ZnO-based materials synthesized via precipitation and hydrothermal methods, where crystal growth and particle aggregation during synthesis and thermal treatment limit the development of porosity.

The relatively low surface area may impose limitations on the availability of active sites and mass transfer processes. However, in the present system, photocatalytic activity is primarily governed by interfacial charge transfer processes rather than surface area alone. In particular, the incorporation of Ti_3C_2Tx MXene promotes efficient electron extraction from ZnO, while the Ce^{4+}/Ce^{3+} redox couple facilitates charge separation. Therefore, despite the modest BET values, enhanced photocatalytic performance is achieved due to improved electronic interactions within the heterostructure.

Similar behaviour has been reported in MXene-based photocatalysts, where charge separation efficiency plays a more dominant role than textural properties.

The optical properties of the synthesized samples were investigated using UV–Vis diffuse reflectance spectroscopy (DRS) to evaluate their light absorption behaviour. Fig. 2 reports the UV–Vis spectra of all the prepared materials: pure MXene and pure ZnO, as well as the MXene_ZnO and MXene_CeO_2_ZnO heterojunctions synthesized through both the precipitation and hydrothermal methods. DR-UV-Vis spectra of the as prepared material show the typical valence band – conduction band transition of ZnO [15], apart from the spectrum of the MXene system, which is completely black, and could not be measured directly with this spectroscopic technique. To enable spectral acquisition, the MXene was diluted with $BaSO_4$ at a 1:10 wt ratio prior to measurement. Consequently, the observed band gap in the DR-UV-Vis spectra of MXene samples corresponds to barium sulphate. For all other samples, the

Table 1
BET values for synthesized samples.

Sample	BET surface area (m^2/g)
MXene	8 ± 2
ZnO_P	20 ± 3
CeO_2_ZnO_P	31 ±0 .3
MXene_ZnO_P	12 ± 2
MXene_ZnO_H	10 ± 2
MXene_CeO_2_ZnO_P	15 ± 3
MXene_CeO_2_ZnO_H	11 ± 2

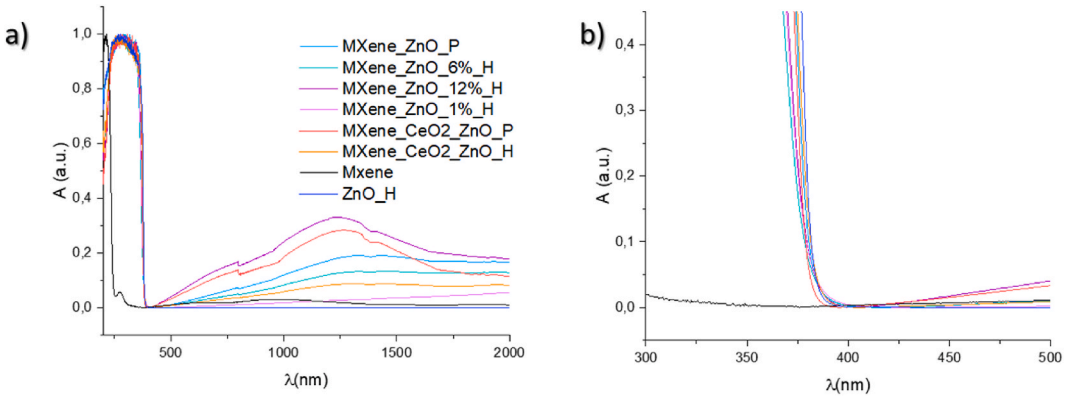

Fig. 2. UV–Vis diffuse reflectance spectra (DRS) of pure MXene, ZnO, MXene_ZnO, and MXene_CeO_2_ZnO samples synthesized via hydrothermal and precipitation methods: (a) full spectral range (200–2000 nm) and (b) magnified view in the 300–500 nm region. The absorption edge at ~3.2 eV corresponds to ZnO band gap transitions, while the broad absorption in the visible–NIR region (400–1200 nm) is attributed to the plasmonic response of MXene.

optical band gap can be attributed to ZnO, using the Tauc method [23], resulting in a value of approximately 3.2 eV, in good agreement with the value of 3.3 eV reported in literature [24] and with our own calculations of the band structure (Fig. S2). The only evidence of the presence of MXene is the plasmonic absorption arising at 400 nm and with a maximum around 1200 nm. This behaviour is amplified in the composite system containing the highest amount of MXene, followed by the mixed sample obtained via precipitation. MXene itself shows an increasing absorption starting from 400 nm, although lower than that of the composite systems. As expected, the samples that absorb the least in the visible range are pure ZnO and the system with the lowest MXene content.

A key aspect in the characterization of this class of 2D materials is the analysis of their morphology. To examine the surface features of the synthesized samples, Field Emission Scanning Electron Microscopy (FESEM) was employed. Fig. 3 shows six representative specimens: the two pristine MXene materials obtained via hydrofluoric acid (HF) etching at concentrations of 10%, two heterojunction systems, namely MXene_ZnO_P and MXene_ZnO_H (where the amount of MXene is 6% wt) and the co-mixed ones MXene_CeO_2_ZnO_P and MXene_CeO_2_ZnO_H. The FESEM pictures of the samples prepared via hydrothermal process and with different loading of MXene (1 and 12%) are reported in Fig. S3. In the case of higher amount of MXene it is possible to observe the formation of the accordion like structure of MXene that completely disappears for lower loading.

As illustrated in Fig. 3a and b (enlargement of 3a), the MXene sample synthesized with 10% HF displays the characteristic "accordion-like" morphology typical of MXene structures [25,26] clearly highlighting the 2D layered architecture.

Conversely, Fig. 3c, d, 3e and 3f show that the MXene_ZnO_H/P and MXene_CeO_2_ZnO_H/P composite features respectively a surface entirely covered by ZnO and by ZnO/CeO_2 particles, which mask the underlying accordion-like structure. This complete coverage results from the synthesis method, which promotes uniform deposition of oxide particles across the MXene surface. The presence of cerium oxide (only 1% molar respect to the concentration of ZnO) together with ZnO has been highlighted by the EDS maps (Fig. S4). This image shows that cerium oxide is well dispersed across the surface of both ZnO and MXene.

Electron Paramagnetic Resonance (EPR) analysis was employed to investigate the paramagnetic species present within the synthesized materials. This technique is particularly valuable for studying photocatalytic systems, as their activity is governed by processes involving the generation, separation, and transfer of charge carriers (electrons and holes), which frequently give rise to paramagnetic centres. The high sensitivity of EPR enables the detection of structural defects: including vacancies, interstitials, and impurities, those act as trapping sites for charge carriers, thereby influencing both their recombination dynamics and their availability to participate in redox reactions at the material surface. The EPR spectra shown in Fig. 4a for the MXene_ZnO_H sample reveal two main resonance signals, indicative of intrinsic defects that give rise to paramagnetic centres. The first signal, with a *g*-value of approximately 1.96, is attributed to electrons trapped in ZnO-related defects. These trapped electrons may participate in the reduction of Zn^{2+} to Zn^{+}; the latter, being electronically unstable, manifests as a detectable paramagnetic species. This response has been previously reported and discussed in the literature [15]. The second signal, centered at $g \approx 2.003$, originates from unpaired electrons trapped at structural defects which are detectable by EPR generated during the synthesis procedure and generally unavoidable in any preparation. At low temperature (77 K), a significant increase in signal intensity is observed compared with room-temperature (RT) spectra. This enhancement arises from the paramagnetic nature of the sample. Since EPR detects microwave-induced spin transitions, a larger population imbalance results in a correspondingly stronger signal.

Subsequently, the sample was irradiated using a high-intensity UV–Vis lamp (filter at 365 nm) Irradiation with photons of energy higher than the ZnO bandgap (Eg ≈ 3.2 eV) promotes electrons from the valence band (VB) to the conduction band (CB). In principle, the photogenerated charge carriers should increase the concentration of paramagnetic centres in zinc oxide (Zn^{+} and O^{-}) as widely demonstrated and described by some of us in a previous paper [15]. However, the presence of MXene, owing to its intrinsic electronic conductivity, efficiently captures the photogenerated electrons, thereby preventing the formation of additional paramagnetic species and stabilizing the ZnO phase. This behaviour is confirmed by the EPR spectra shown in Fig. 4b, where comparison of the signals before and after irradiation reveals no detectable changes in either shape or intensity.

Fig. 5a shows the EPR spectra of the MXene_CeO_2_ZnO_H sample. The spectra appear essentially identical to those of the MXene_ZnO_H sample reported in Fig. 4a, not because cerium oxide lacks paramagnetic character, but due to the nature of its EPR response. The unpaired electron in the 4f orbital of the Ce^{3+} ion gives rise to an EPR signal that is effectively "silent," meaning that it is not easily detected because it is broadened over the entire spectral range. This broadening is a consequence of the large spin–orbit coupling constant of the cerium atom. Indirect evidence of the "silent" EPR signal associated with Ce^{3+} is provided in Fig. 5b, which compares the EPR spectra of the sample before and after irradiation. The post-irradiation spectrum exhibits a noticeable decrease in signal intensity. Under irradiation, one would expect the formation of trapped electrons in the form of Zn^{+} centres; however, the presence of Ce^{4+} ions enables efficient electron capture, leading to their reduction to Ce^{3+}. Since the EPR signal of Ce^{3+} is effectively "silent" due to its extensive spectral broadening, this

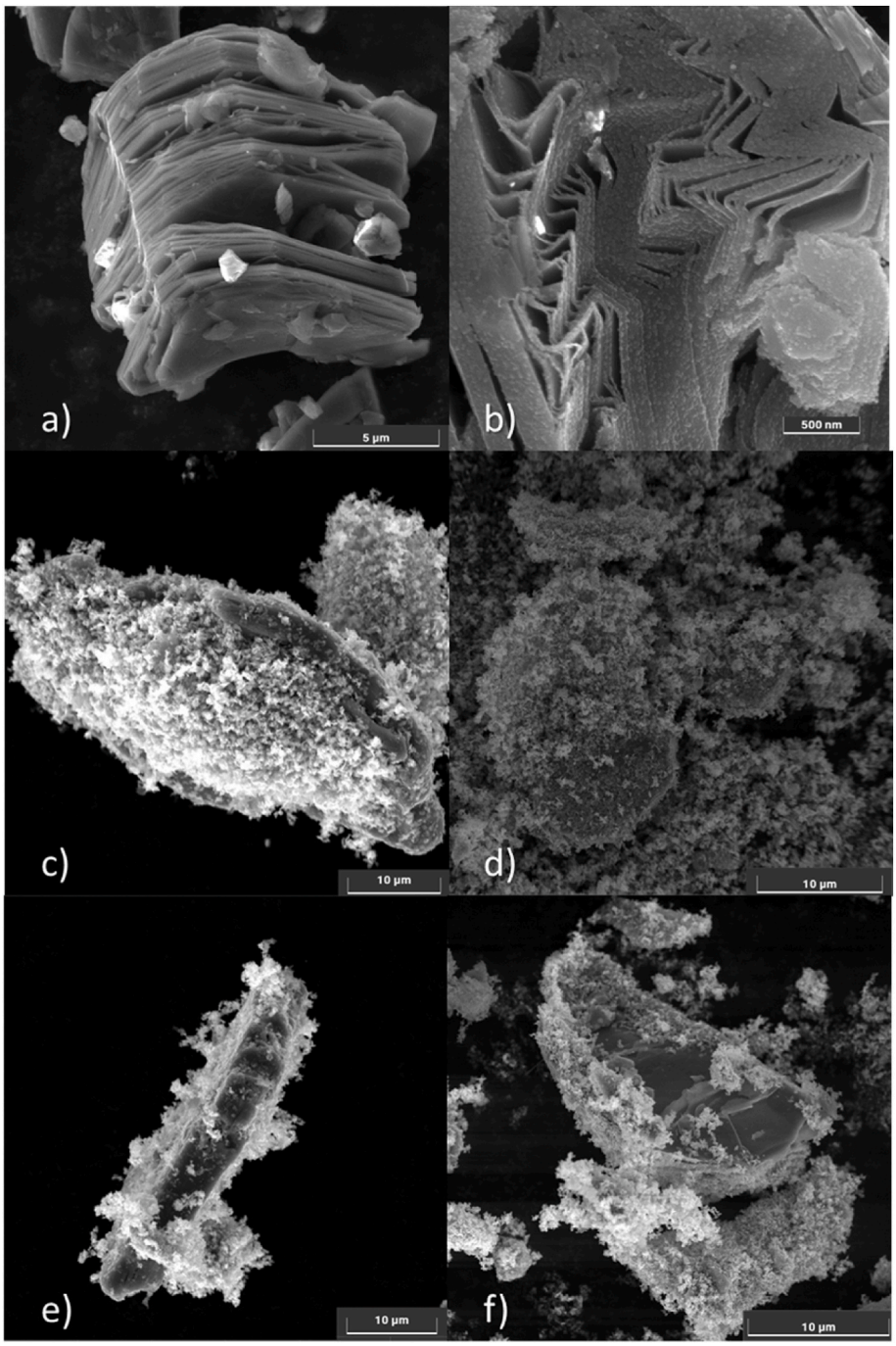

Fig. 3. FESEM images of (a–b) pristine MXene showing the characteristic accordion-like layered morphology, (c–d) MXene_ZnO composites synthesized via hydrothermal (c) and precipitation (d) methods, and (e–f) MXene_CeO_2_ZnO composites obtained via hydrothermal (e) and precipitation (f) routes.

electron-trapping process results in a reduced intensity of the EPR signal attributed to Zn^{+}. In this case the electron transfer from ZnO to other matrices (CeO_2 and MXene surfaces) is more efficient than in the case of the two component sample MXene_ZnO. The presence of Cerium with its ability to capture and stabilize electrons is even improved by the presence of MXene.

X-ray photoelectron spectroscopy (XPS) was employed to investigate the surface chemistry of the MXene-based composites. Core-level spectra were analyzed to determine the chemical states of the elements present.

The survey spectra of all samples (Fig. 6) confirm the successful incorporation of secondary phases onto the MXene surface. In addition to the Ti, C, O, and F signals characteristic of MXene, the MXene/ZnO and MXene/ZnO-CeO_x composites show clear Zn signals, while the Ce contribution is not clearly distinguishable. Residual amounts of Al, originating from the MAX phase, were detected only in the pure MXene sample (see Table 2).

The relative atomic concentrations, reported in Table 1 and obtained from the integration of high-resolution core-level spectra, reveal a surface strongly enriched in O, C, and Zn. Except for the bare MXene, where the Ti signal is clearly visible (18.4 at.%), Ti is nearly undetectable in the other samples from the survey scans, and prolonged high-resolution acquisitions were required to obtain reliable signals for each region.

This behavior reflects both the high surface reactivity of the MXene and the coverage provided by ZnO or ZnO–CeO_x, as previously confirmed by SEM analysis. The elevated oxygen content suggests partial surface oxidation of the MXene sheets, a phenomenon commonly

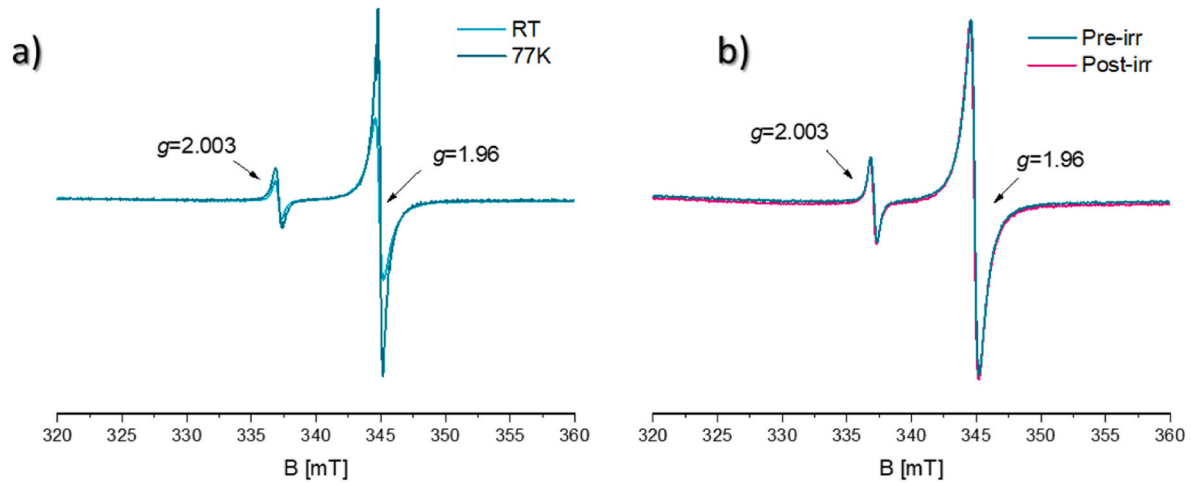

Fig. 4. X-band CW-EPR spectra of the MXene_ZnO_H sample: (a) comparison between room temperature (RT) and 77 K, showing enhanced signal intensity at low temperature due to increased spin population; (b) spectra before and after UV irradiation (365 nm) recorded at 77K.

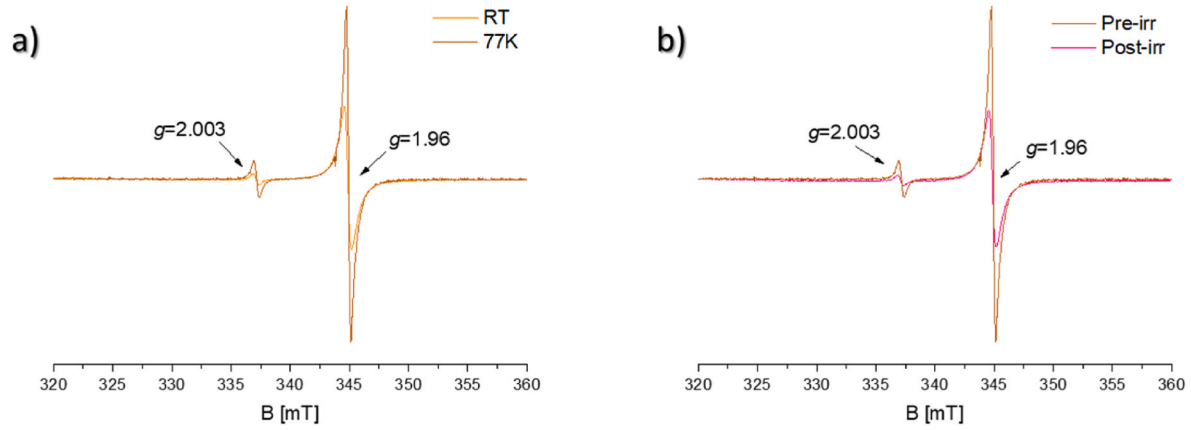

Fig. 5. X-band CW-EPR spectra of the MXene_CeO_2_ZnO_H sample: (a) comparison between room temperature and 77 K; (b) spectra before and after UV irradiation (365 nm) recorded at 77K.

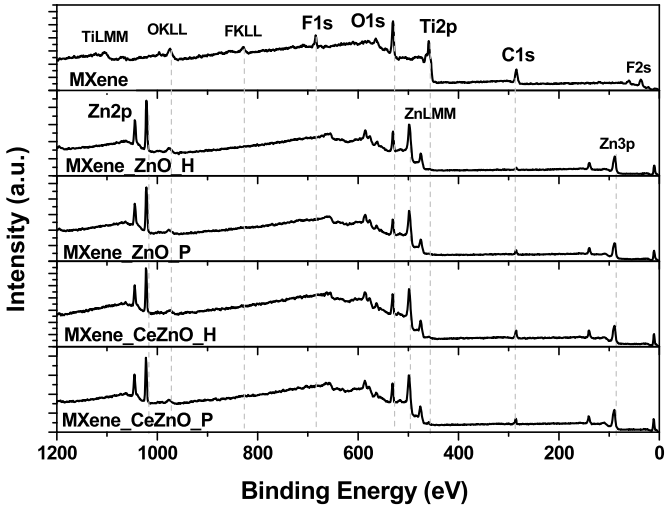

Fig. 6. XPS survey spectra of pure MXene, MXene_ZnO, and MXene_CeO_2_ZnO samples synthesized via hydrothermal and precipitation methods. The spectra confirm the presence of Ti, C, O, and F signals characteristic of MXene, along with Zn contributions in the composites. The weak or barely detectable Ti signal in the composites reflects surface coverage by oxide phases and partial oxidation of MXene, consistent with SEM observations.

Table 2
XPS relative atomic concentrations (at.%) calculated from HR spectra.

SAMPLE	Atomic concentration [at.%]						
	C1s	O1s	Ti2p	F1s	Al2s	Zn2p3	Ce3d
Mxene	38.4	34.2	18.4	7.5	1.5	/	/
Mxene_ZnO_H	9.7	59.9	2.0	0.7	/	27.7	/
Mxene_ZnO_P	25.8	44.7	1.6	1.0	/	26.9	/
Mxene_Ce_ZnO_H	32.0	43.7	1.3	/	/	22.5	0.4
Mxene_Ce_ZnO_P	25.3	51.1	1.9	/	/	21.2	0.5

observed in $Ti_3C_2T_x$ exposed to air or aqueous environments [27].

Starting from the bare MXene sample, both the C 1s and Ti 2p regions were analyzed to evaluate the oxidation states. The high-resolution C 1s spectrum (Fig. 7, left) exhibits a rather complex structure. Beginning with the lowest binding energy components, the characteristic MXene "fingerprint" peak appears at 281.9 eV. Adjacent to this, at 282.4 eV, is the contribution associated with F terminations on the MXene surface (C–Ti–T_x), followed by the component at 283.4 eV attributed to passivated surface species (C–Ti–O_x).

At approximately 285 eV, the contribution from adventitious carbon contamination is observed, while a prominent peak at 286.7 eV is assigned to C–OH/C–O surface terminations. The final two components, located at 289.0 and 290.8 eV, correspond to C═O and O–C═O groups, respectively [28].

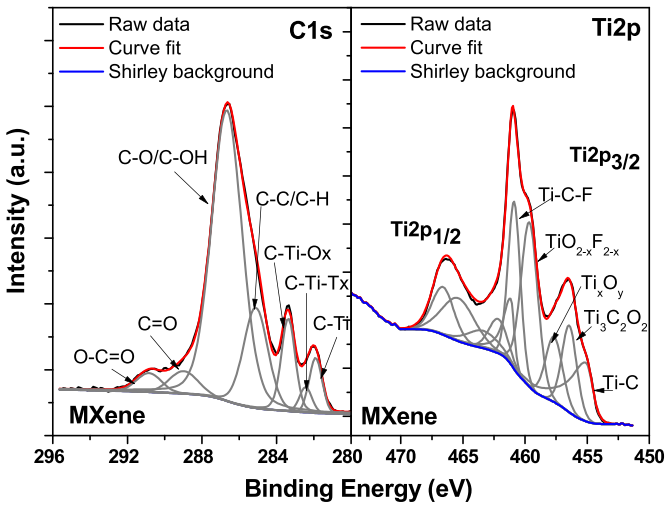

Fig. 7. High-resolution XPS spectra of pristine MXene: (left) C 1s region and (right) Ti 2p region. The C 1s spectrum shows the characteristic Ti–C component at ~281.9 eV, along with contributions from surface terminations (C–Ti–O_x, C–OH/C–O) and oxidized carbon species (C═O, O–C═O).

The same analysis performed on the ZnO-based composites (not shown) reveals C 1s regions dominated by adventitious carbon and surface C–O species, as expected for oxide-based systems. Consequently, the carbide-related C–Ti signal expected at ~281.8–282.0 eV is either very weak or not clearly distinguishable, consistent with the strong surface oxidation of the MXenes.

The Ti 2p region (Fig. 7, right) of the pure MXene sample also displays a complex structure. This behavior is widely reported in the literature and arises from the large surface area of the material, its high reactivity, and the presence of surface passivation due to both oxidation and residual species from the chemical exfoliation of the MAX phase. In particular, functionalization with residual F and Al atoms, not completely removed during HF treatment, contributes to this complexity.

As highlighted in the detailed study by Brette et al. [16], it is essential to consider not only the chemical environment of surface atoms but also that of bulk atoms probed by XPS (within a nominal depth of ~10 nm). Furthermore, the nature of the chemical bonds—specifically interatomic distances—plays a key role in determining chemical shifts, which are often misinterpreted. Surface bonds are particularly sensitive to these effects, especially in the presence of oxidation, leading to a shift of the Ti_xC_y component of about 1.52 eV, from 453.7 eV for Ti_3C_2 to 455.2 eV for $Ti_3C_2O_2$.

Based on this framework and previous literature [29], the deconvoluted Ti 2p spectrum of the pure MXene was assigned as follows: 455.1 eV to Ti–C (MXene), 456.4 eV to $Ti_3C_2O_2$, 457.7 eV to Ti_xO_y, 459.6 eV to $TiO_{2-x}F_{2-x}$, and 460.9 eV to Ti–C–F surface species.

The Ti 2p region was also analyzed for the ZnO-based composites. As clearly shown in Fig. 8, a common behavior is observed for the hydrothermally synthesized samples, both with and without Ce: a small contribution at lower binding energy, associated with carbide species, is still detectable. In contrast, the samples prepared via the precipitation method exhibit a simpler Ti 2p doublet, mainly related to Ti^{3+}/Ti^{4+} components in the 457–459 eV range, while the characteristic carbide-related Ti–C signal at ~455 eV is strongly suppressed or not detectable. This indicates that, regardless of the secondary phase, the MXene surface is largely converted into TiO_x, leading to the formation of a Ti_3C_2@TiO_x core–shell structure. Due to the low intensity of the Ti 2p signal and its overlap with the tail of the Zn LMM Auger peak (located on the left side of the peaks) these regions were not deconvoluted.

The Zn 2p spectra of the MXene/ZnO-based composites (Fig. 9, left)

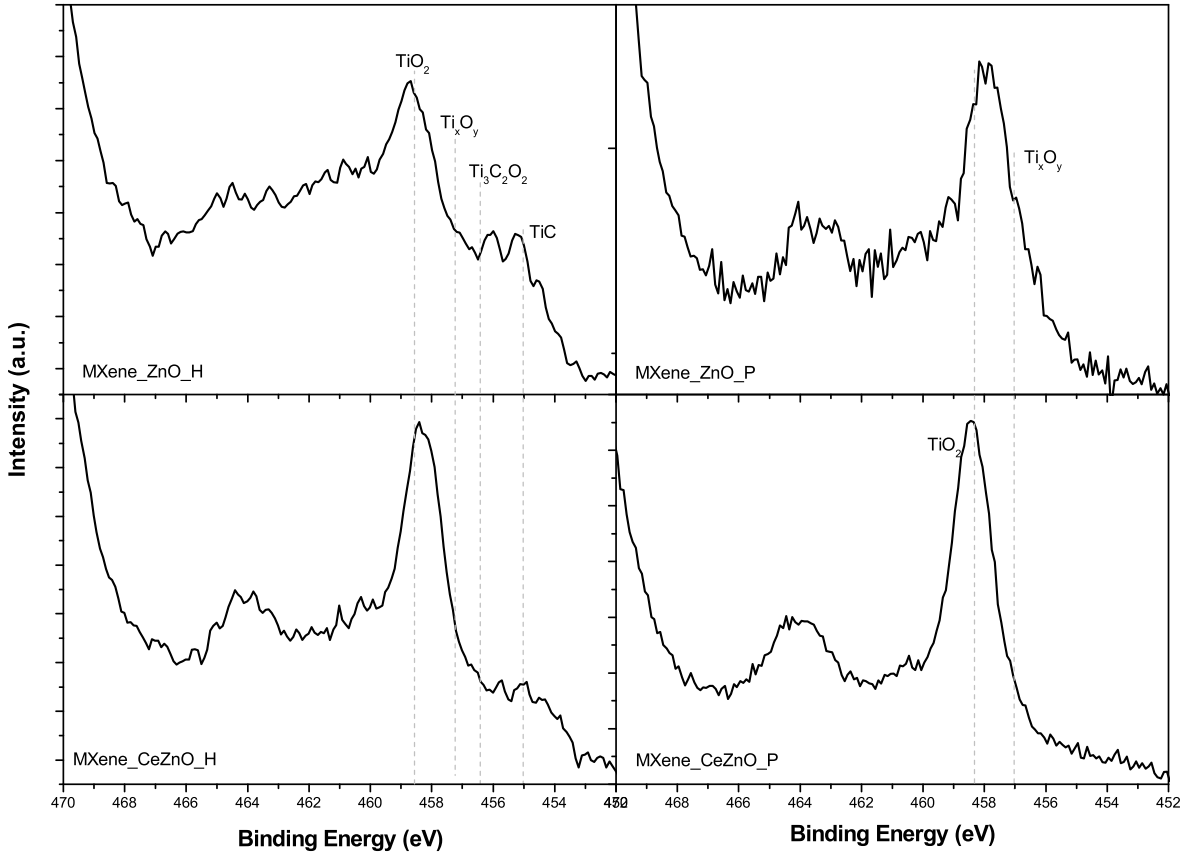

Fig. 8. High-resolution XPS Ti 2p spectra of MXene-based composites synthesized via hydrothermal and precipitation methods.

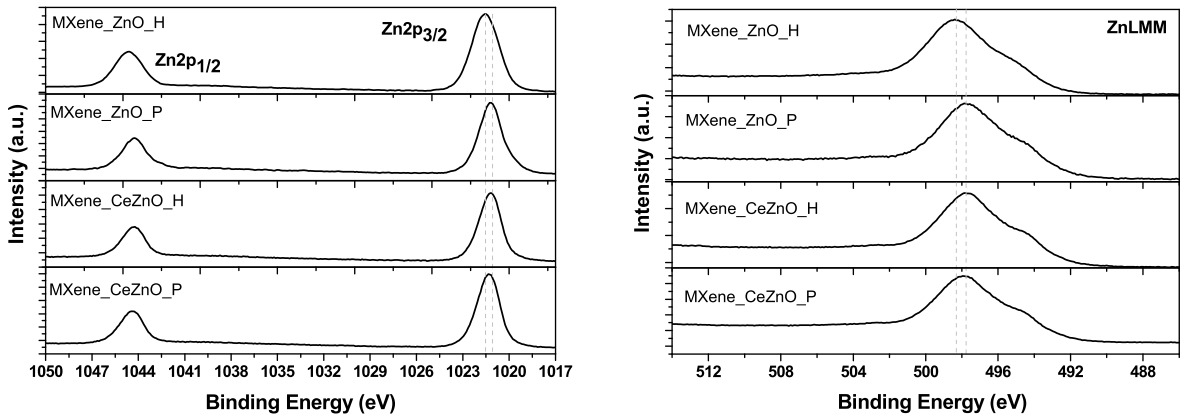

Fig. 9. High-resolution XPS spectra of Zn-containing samples: (left) Zn 2p region and (right) Zn LMM Auger region. The Zn $2p_{3/2}$ peak at ~1021.2–1021.5 eV confirms the presence of Zn^{2+} species characteristic of ZnO. The corresponding Zn LMM Auger features allow determination of the Modified Auger Parameter (MAP), indicating predominantly ZnO character with minor contributions from $Zn(OH)_2$ in selected samples. No evidence of metallic Zn is observed.

show a well-defined Zn $2p_{3/2}$ peak in the range 1021.2 eV (MXene–ZnO_P, MXene–CeZnO_H) to 1021.5 eV (MXene–ZnO_H), which is characteristic of Zn^{2+} [30]. No additional components associated with metallic Zn or other species are detected, indicating that zinc is predominantly present in the oxide form.

To further confirm this interpretation, the Zn LMM Auger regions were also analyzed for each sample (Fig. 9, right). In this case as well, the spectra are very similar, with only slight shifts observed, resulting in main peak positions in the 498.4–497.8 eV range.

By combining the Zn $2p_{3/2}$ and Zn LMM peak positions, it is possible to evaluate the Modified Auger Parameter (MAP), which is independent of the chosen binding energy reference since it relies on the relative energy difference between these two features. According to Duchoslav et al. [31], the expected MAP value for ZnO is (2010.1 ± 0.1) eV. In this work, a value of 2010.0 eV was obtained for the MXene–ZnO_P, MXene–CeZnO_P, and MXene–CeZnO_H samples, while a slightly lower value of 2009.7 eV was measured for MXene–ZnO_H.

Considering that the Zn $2p_{3/2}$ binding energy for $Zn(OH)_2$ is 1021.6 eV, with a corresponding MAP value of 2009.1 eV, these results suggest that the MXene–ZnO_H sample exhibits a surface composition that can be described as a mixture of ZnO and $Zn(OH)_2$ phases.

The final analysis was devoted to the high-resolution Ce 3d spectra of the MXene/ZnO–CeO_x composites (Fig. 10). Due to the very low concentration of Ce, each acquisition required more than 300 min in order to obtain spectra with sufficient signal-to-noise ratio for reliable interpretation of the oxidation states.

Based on the detailed study by K. I. Maslakov et al. [32], six peaks were assigned to Ce^{4+} species (v, v″, and v‴ for the Ce $3d_{5/2}$ component, and u, u″, and u‴ for the Ce $3d_{3/2}$ component), while four peaks were attributed to Ce^{3+} (v^0 and v′ for Ce $3d_{5/2}$, and u^0 and u′ for Ce $3d_{3/2}$).

The MXene–CeZnO_P sample (Fig. 10, bottom) exhibits only the characteristic features of Ce^{3+} species, with no detectable contribution from Ce^{4+}. In particular, the peak typically observed at ~916 eV (u‴), commonly considered the fingerprint of Ce^{4+} [33], is absent. This indicates that cerium is present at the surface exclusively in a reduced oxidation state, consistent with a Ce_2O_3-like phase.

In contrast, the MXene–CeZnO_H sample shows contributions from both Ce^{3+} and Ce^{4+} oxidation states, requiring a fitting procedure with ten components, as illustrated in Fig. 10 (top).

These findings demonstrate that different synthesis methods lead to distinct surface chemistries, which can significantly influence the behavior of these materials in catalytic applications, where surface properties play a crucial role.

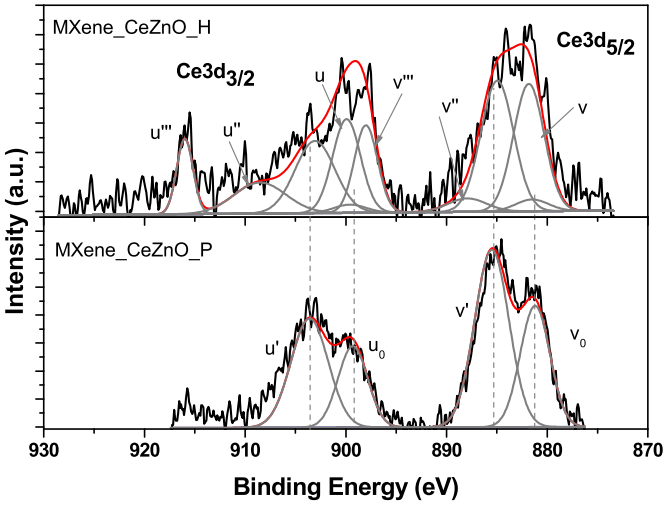

Fig. 10. High-resolution XPS Ce 3d spectra of MXene_CeZnO samples synthesized via (top) hydrothermal and (bottom) precipitation methods. The hydrothermal sample exhibits both Ce^{3+} and Ce^{4+} components, as evidenced by the presence of characteristic multiplet features, including the Ce^{4+} fingerprint peak at ~916 eV. In contrast, the precipitation-derived sample shows predominantly Ce^{3+} species, with no detectable Ce^{4+} contribution. These results indicate a mixed-valence cerium surface in the hydrothermal sample, consistent with its role as a redox-active electron buffer.

3.2. Hydrogen production

After completing the calibration of the analytical setup, preliminary photocatalytic hydrogen production tests were conducted on the synthesized materials to evaluate their ability to promote water-splitting reactions under controlled conditions. Hydrogen evolution was assessed by irradiating the various synthesized materials with a UV lamp set at 365 nm. A comparative analysis of the H_2 ion currents reveals clear differences in their photocatalytic activity. To obtain normalized and comparable data across all samples, the measured H_2 ion current was converted into micromoles of hydrogen produced per gram of material per hour ($\mu mol \bullet g^{-1} \bullet h^{-1}$) using the calibration curve. For what concern the performances, under UV irradiation (filter at 365 nm), all samples (except for pure ZnO) exhibit a progressive increase in H_2 generation, with a general tendency toward stabilization after approximately 20 min and a plateau for the rest of the 1-h experiment. Only the data corresponding to the most relevant samples are reported in Fig. 11. Specifically, the ZnO_H, MXene_6%_ZnO_H, MXene_1%_ZnO_H, MXene_12%

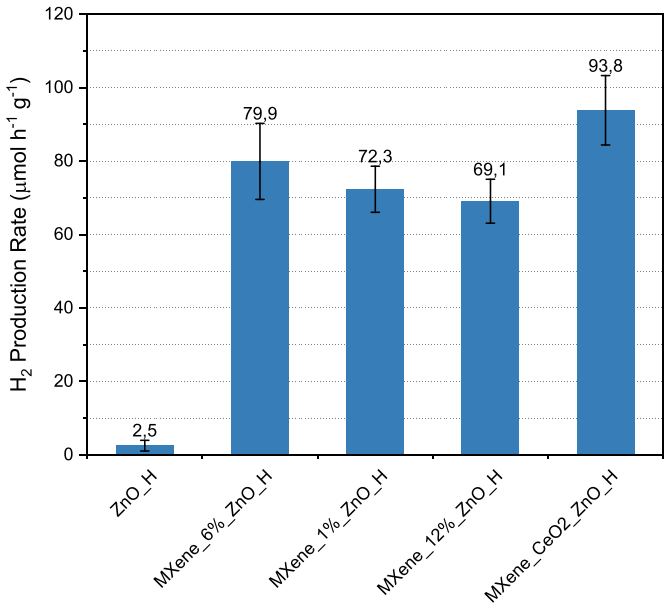

Fig. 11. Bar chart of the photocatalytic hydrogen evolution rates (μmol g^{-1} h^{-1}) under UV irradiation (365 nm, 4 W) for selected samples. The MXene_CeO_2_ZnO_H sample exhibits the highest activity (93.8 μmol g^{-1} h^{-1}), outperforming both the binary MXene_ZnO_H system and pure ZnO. Error bars represent uncertainties derived from calibration and signal stability.

_ZnO_H, and MXene_CeO_2_ZnO_H samples are shown, as these exhibited the most comparable hydrogen production rates of 2.5 μmol•g^{-1} h^{-1}, 79.9 μmol•g^{-1} h^{-1}, 72.3 μmol•g^{-1} h^{-1}, 69.1 μmol•g^{-1} h^{-1}, and 93.8 μmol•g^{-1} h^{-1}, respectively. Only the data corresponding to the best-performing samples are reported in Fig. 6. Specifically, the MXene_6%_ZnO_H, MXene_1%_ZnO_H, and MXene_12%_ZnO_H samples are shown, as these exhibited the highest and most comparable hydrogen production rates. In contrast, all samples synthesized via the precipitation method consistently showed lower H_2 production (not reported) throughout the tests compared with those prepared using the hydrothermal route, also we did not obtained results for the pure MXene sample. This suggests that the method used to prepare the heterojunctions may influence the quality of the MXene/ZnO interface. The observed differences in photocatalytic performance between the samples prepared via precipitation and hydrothermal methods suggest that the synthesis route influences the properties of the resulting materials. However, it should be noted that the experimental conditions associated with the two methods are not strictly identical, particularly in terms of temperature and reaction environment. These differences may affect several key factors, including the crystallization degree of ZnO and CeO_2, the dispersion and structural preservation of MXene, and the nature and distribution of its surface functional groups. In particular, hydrothermal synthesis is generally associated with more controlled crystal growth and improved interfacial contact between components, which may favour more efficient charge transfer across the MXene/ZnO interface. Conversely, the precipitation method may lead to a less homogeneous distribution of phases, as well as a higher degree of structural disorder or partial oxidation of MXene, especially during subsequent thermal treatment. These effects can influence both the electronic properties of MXene and the quality of the heterojunction interface. Therefore, the differences in photocatalytic activity observed in this work are interpreted as arising from a combination of factors, including interfacial contact, MXene structural retention, and synthesis-induced modifications of the oxide phases, rather than from a single parameter. At the same time, it is important to emphasize that a fully controlled comparison isolating the effect of synthesis parameters was not possible within the scope of this study. A more systematic investigation, involving independently controlled synthesis variables and advanced interfacial characterization techniques, would be required to quantitatively assess the impact of preparation method on the MXene/ZnO interface. This aspect will be addressed in future work. Pure MXene ($Ti_3C_2T_x$) does not produce H_2 under irradiation because it lacks a suitable bandgap for visible-light absorption and suffers from rapid charge carrier recombination, despite its metallic conductivity and electron-accepting properties. In MXene/ZnO or MXene/ZnO–CeO_2 hybrids, ZnO (bandgap ~3.2 eV) acts as the primary photocatalyst, generating electron-hole pairs upon UV/visible irradiation [8]. The intimate heterojunction interface forms a Schottky barrier or Type-II alignment, where MXene's high work function (~4.5-5 eV) and conductivity trap photogenerated electrons from ZnO's conduction band, suppressing e^--h^+ recombination and directing electrons to surface protons for H_2 evolution ($2H^+ + 2e^- \rightarrow H_2$) [34].

CeO_2 addition in ZnO_CeO_2 creates oxygen vacancies and mixed valence states (Ce^{3+}/Ce^{4+}), improving charge separation and light harvesting; MXene further boosts electron transfer, yielding synergistic H_2 rates up to 10x higher than singles [35]. This explains referee requests for revisions: likely to clarify bandgap/CB positions, prove interface effects (e.g., via XPS, EIS), and quantify why pure MXene yields zero H_2 while hybrids excel [36].

The enhanced photocatalytic performance observed upon incorporation of CeO_2 can be attributed to the presence of the Ce^{4+}/Ce^{3+} redox couple, which plays a key role in charge separation. This redox process is reversible and can be described by the equilibrium:

$$Ce^{4+} + e^- \rightleftharpoons Ce^{3+}$$

Under irradiation, photogenerated electrons from ZnO can be trapped by Ce^{4+} species, leading to the formation of Ce^{3+}. This process effectively suppresses electron–hole recombination by temporarily storing electrons. Subsequently, Ce^{3+} can be reoxidized back to Ce^{4+} through electron transfer to adsorbed species involved in hydrogen evolution, thereby restoring the initial state of the material. Therefore, CeO_2 acts as a dynamic electron buffer within the heterostructure, enhancing charge separation without undergoing irreversible transformation. This reversible redox cycling is widely reported in CeO_2-based photocatalytic systems and is associated with the presence of oxygen vacancies that facilitate electron mobility. Although partial surface modification of CeO_2 under reaction conditions cannot be completely excluded, the Ce^{4+}/Ce^{3+} redox process itself does not lead to catalyst degradation, but rather contributes to maintaining photocatalytic activity through continuous charge transfer.

Finally, within the MXene_ZnO series, the MXene_6%_ZnO_H sample shows the best performance, indicating that it has the most favourable ratio of MXene to ZnO. However, when considering all samples, the MXene_CeO_2_ZnO_H mixed system exhibits the highest photocatalytic activity overall. The MXene-based composites have recently gained prominence as efficient photocatalysts for solar-driven hydrogen production. Their high electrical conductivity and tuneable surface chemistry enable enhanced charge separation and accelerated electron transport, thereby reducing recombination losses. In our case, coupling with ZnO and forming ternary systems such as ZnO_CeO_2 promotes stronger interfacial contact, improved light harvesting, and charge transfer. This improved charge transfer enhances the rate at which the photocatalytic steps on both the MXene and ZnO (100) surfaces proceed, resulting in the observed higher performance. Among all investigated samples, the MXene_CeO_2_ZnO_H system exhibits the highest photocatalytic activity, with a hydrogen evolution rate of 93.8 μmol g^{-1} h^{-1} under the adopted experimental conditions. This value represents a significant enhancement compared to the other investigated systems. In particular, the hydrogen production rate is approximately ~37 times higher than pure ZnO, which shows negligible activity under the same conditions, and about ~1.2 times higher than the binary MXene_ZnO_H sample, highlighting the beneficial effect of introducing CeO_2 into the

heterostructure. The amount of hydrogen produced is consistent with values reported in the literature [37], particularly considering that ethanol was used as the hole scavenger, which is known reduce photocatalytic performance. It is important to note that the use of ethanol instead of more standard sacrificial agents such as methanol or triethanolamine may lead to a systematic underestimation of the hydrogen evolution rate, due to slower hole-scavenging kinetic. In Table 3 a comparison with representative literature systems has been proposed to place our results in the broader context of MXene-based photocatalysis.

A comparison with representative MXene/oxide systems reported in the literature is presented in Table 3. Although direct comparison is not straightforward due to differences in light sources, reactor configurations, and sacrificial agents, the hydrogen evolution rate obtained in this work (93.8 μmol g^{-1} h^{-1}) falls within the expected range for MXene/oxide-based photocatalysts under mild irradiation conditions. For instance, MXene/TiO_2 systems typically exhibit hydrogen production rates in the range of 200–350 μmol g^{-1} h^{-1} under high-power xenon irradiation and using methanol as sacrificial agent, while MXene/ZnO-based systems can reach higher values when sulfide/sulfite hole scavengers are employed. Therefore, considering the relatively low irradiation power (4 W UV lamp) and the use of ethanol, the performance of the present system can be regarded as competitive within this class of materials.

The choice of sacrificial agent plays a crucial role in determining the efficiency of photocatalytic hydrogen evolution. In the present study, ethanol was selected due to its lower toxicity and safer handling compared to methanol. However, it is well established in the literature that methanol generally leads to higher hydrogen evolution rates due to its simpler oxidation pathway and faster kinetics. Quantitatively, several studies on oxide-based and MXene-based photocatalysts report that the use of ethanol instead of methanol can result in a reduction of hydrogen evolution rates in the range of ~10–30%, depending on the catalyst system and experimental conditions. This difference is attributed to the more complex multi-step oxidation pathway of ethanol, involving intermediates such as acetaldehyde and acetic acid, which slow down hole scavenging and reduce electron availability for hydrogen evolution. Therefore, the hydrogen production rate measured in this work should be considered a conservative estimate, and higher values could reasonably be expected under standard benchmarking conditions using methanol or triethanolamine.

3.3. Water splitting mechanism

The reaction coordinate diagram describing water oxidation on ZnO (100) is depicted in Fig. 12. Water adsorbs weakly onto the ZnO surface ($\Delta G = -0.03\ eV$, *I*, Fig. 12), stabilised by a hydrogen bond to the opposing oxygen bridge site. The first dissociation proceeds via O–H heterolytic bond cleavage, yielding OH^- and H^+ through an exergonic

Table 3
Comparison between experimental data of H_2 production.

Materials	Light source	Sacrificial agent	H_2 evaluation	Article
Ag/ZnO	300W Hg–Xe lamp	ethanol	805 μmol/h*g	[38]
Ti_3C_2/ZnO 2D/0D	300W Xenon Lamp	0.25 M $Na_2SO_3{\cdot}6H_2O$ and 0.35 $Na_2S{\cdot}9H_2O$	709 μmol/h*g	[36]
TiO_2/Ti_3C_2	300W Xenon lamp	25% Ethanol	218 μmol/h*g	[39]
urchin-like TiO_2/$Ti_3C_2O_x$	300W Xenon Lamp	20% methanol	347 μmol/h*g	[40]
Ti_3C_2/ZnO/CeO_2	**Uv lamp 4W**	**10% ethanol**	**93.8 μmol/h*g**	**This work**

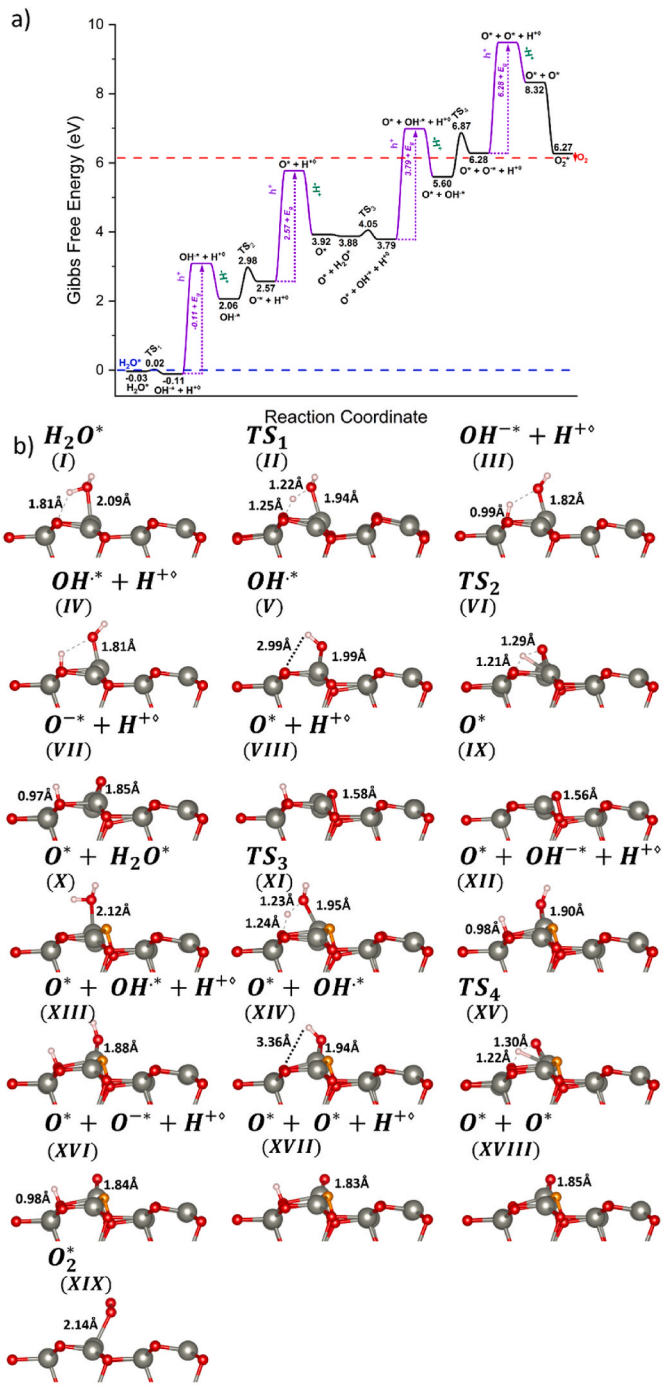

Fig. 12. (a) Reaction coordinate diagram for the overall solvated water splitting process on the (100) wurtzite ZnO surface. Protons bind to O_{surf} sites, whereas all other surface species bind to Zn_{3c}^{2+} sites. Gibbs free energies are shown as black lines. Purple lines indicate the gain or loss of charge carriers or protons: uphill steps on the diagram correspond to the photogeneration of a hole while downhill steps correspond to the release of a proton from the surface. The energy of the positively charged intermediates, after hole generation and proton loss, is obtained by increasing the energy of the reactant state by the ZnO band gap (E_g = 3.2 eV [46]). Non-adsorbed species are denoted by horizontal blue (water) and red (oxygen) dashed lines. Zn and O_{surf} active sites are represented by the symbols * and ◇, respectively. (b) Optimized structures of adsorbed intermediates and transition states with key bond lengths indicated. Atom colour legend: O (red), Zn (grey), H (light pink). For clarity, the first O* is highlighted in orange from structure X. (For interpretation of the references to colour in this figure legend, the reader is referred to the Web version of this article.)

thermal process (*I-III*, Fig. 12). This step is kinetically facile, with a low forward barrier of 0.05 eV, whereas the backward reaction has a higher barrier of 0.13 eV. The low reaction barrier reflects the stabilizing effect provided by the formed OH^- and the O_{surf} group, which together act to shuttle the proton between sites. However, this dissociation competes with water desorption from the surface, which may reduce the overall activity of the catalyst. The resulting hydroxyl anion (*III,* Fig. 12b) can capture a photogenerated hole to form a hydroxyl radical (*IV*, Fig. 12b). In contrast, the second O–H dissociation step (*VI*, Fig. 12b) is endergonic, exhibiting a forward barrier of 0.92 eV (Fig. 12a), and a backward barrier of 0.41 eV. This reflects the inherent instability of the oxygen anion intermediate, whose small size and poor charge delocalisation make it energetically unstable. Moreover, this pathway is unlikely to dominate in the presence of a sacrificial agent (e.g. methanol, ethanol) since hydroxyl radicals preferentially react with the organic species, thereby consuming surface $OH^\bullet$ species. Upon formation, the oxygen atom bonds with a neighbouring O_{surf} site to produce a surface-bound peroxo intermediate (*IX*, Fig. 12b). Rather than releasing O_2 by forming an oxygen vacancy, a more favourable pathway involves the adsorption of a second water molecule near the peroxo species (*X*, Fig. 12b). This molecule undergoes deprotonation and dissociates through a thermal process analogous to the first deprotonation, but with a higher forward barrier ($\Delta G = 0.17\ eV$). The increase in barrier is attributed to steric hindrance, with the first O adatom constraining the Zn site bound to the second adsorbed water, lengthening the H transfer distance to the O_{surf} site, straining the hydrogen bonds that stabilize the transition state. The resulting OH^- captures a hole to form $OH^\bullet$ (*XIII*, Fig. 12b). However, the cleavage of the radical is strongly disfavoured, with a forward barrier of 1.27 eV and a backward barrier of 0.59 eV, with the increase in barrier likely due to the same steric constraints described above. The two O adatoms are energetically unstable when isolated on the surface but readily recombine on a Zn site to form O_2, which subsequently desorbs. The solvated Gibbs free energy change for water splitting is calculated to be 5.49 eV in the gas phase, and 6.14 eV after including the solvation correction. The inconsistency with the experimentally measured standard Gibbs free energy change (4.92 eV) [41] is related to the systematic error of GGA functionals, and their tendency to overestimate the energy of triplet O_2 [42]. Such deviations are well documented in the literature where calculated reaction energies similarly exceed the thermodynamic limits[43–45]. It is worth noting that these results are therefore intended to support comparative analysis and mechanistic insights, rather than absolute thermodynamic accuracy.

Our calculations indicate that while the O–H cleavage is kinetically and thermodynamically accessible, the subsequent deprotonation of OH species is significantly uphill, leading to a hydroxylated surface. In the presence of a sacrificial agent, the surface hydroxyls are rapidly consumed through a radical assisted dehydrogenation pathway (Fig. 14), displacing water and reducing the build-up of OH species. The formation of heterojunctions with Ti_3C_2, MXene, and CeO_2 enhances the concentration of surface-reaching photogenerated holes, increasing the likelihood that oxidative surface reactions occur before charge recombination. This effect is reflected in the increasing hydrogen production rate observed in Fig. 11. Overall, the photocatalytic hydrogen production rate is primarily governed by the availability and lifetime of these charge carriers rather than by large kinetic barriers. The observed multifold increase in hydrogen production, even for less performing samples can be attributed to the availability of more efficient hydrogen evolution sites provided by MXene.

3.4. Sacrificial agent oxidation mechanism

This section describes the photocatalytic oxidation mechanisms of the sacrificial agent. In this work, methanol was employed as a model organic species in the theoretical calculations to represent the hole scavengers, due to its simple structure, which facilitates computational simulations. Ethanol exhibits slower reacting kinetics compared to methanol as indicated by the comparative adsorption and O–H bond cleavage reaction coordinate diagram depicted in Fig. S9. The following section aims to provide a detailed mechanistic understanding of the oxidation pathway. Methanol adsorbs weakly onto the ZnO surface ($\Delta G = -0.25\ eV$, *I,* Fig. 13b), through hydrogen bonding to a bridging oxygen. The first deprotonation proceeds via an exergonic heterolytic cleavage of the O–H bond, shuttled through the hydrogen bond network between two adjacent O groups. This step proceeds with a forward barrier of 0.27 eV, and a backward barrier being 0.39 eV, yielding a CH_3O^- species (*I-III*, Fig. 13b) bound to a Zn_{3c}^{2+} site with a Zn_{3c}^{2+}–O bond length of 1.83 Å (*III*, Fig. 13b). This reaction is stabilised by strong hydrogen bonding both before and after proton transfer. Subsequent oxidation by a photogenerated hole produces a $CH_3O^\cdot$ radical (*IV*, Fig. 13b), weakening the Zn_{3c}^{2+}–O bond to 1.85 Å. The molecule is favourably reoriented (*IV*, Fig. 13b), resulting in a facile C–H dissociation with a low energy barrier of 0.19 eV. During C–H bond cleavage, the Zn_{3c}^{2+} site accepts an electron from the $CH_3O^\cdot$ species, reducing it to Zn_{3c}^{+}, and weakening the Zn–O bond. After dissociation, the resulting CH_2O molecule rearranges with its CH_2 group oriented away from the terminal hydroxyl group. This structure is highly stable relative to the methoxy radical (Fig. 13a), making this reaction effectively irreversible. Finally, the reduced Zn_{3c}^{+} site can be reoxidized by hole capture, restoring the active site, while the formed CH_2O molecule bridges across adjacent Zn

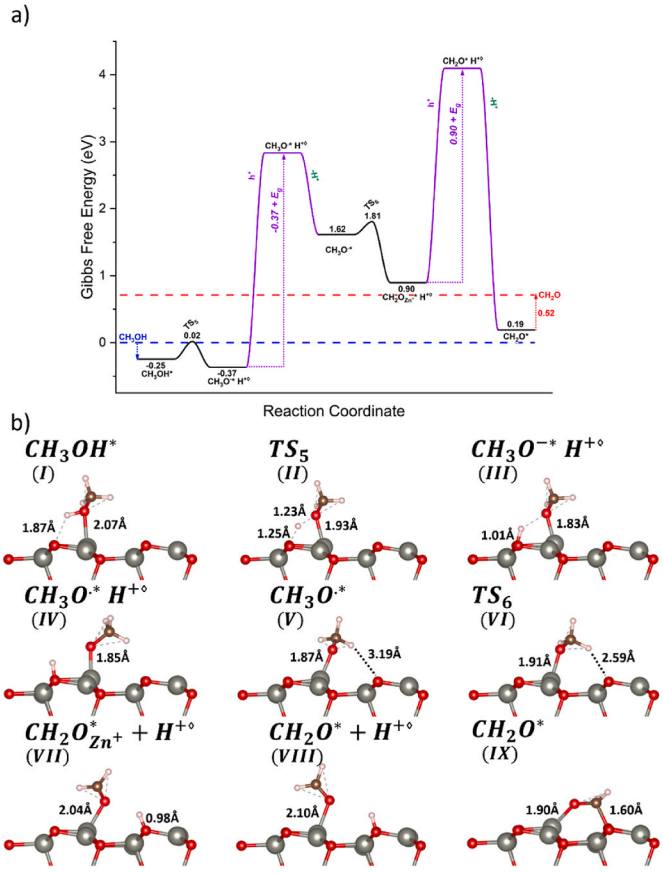

Fig. 13. (a) Reaction coordinate diagram for the solvated oxidation of methanol to formaldehyde over the (100) wurtzite ZnO surface. Adsorbed species bind to Zn_{3c}^{2+} sites unless specified while protons bind to O_{surf} sites. Notation corresponds to Fig. 12, with the dashed lines representing methanol (blue) and formaldehyde (red). (b) Geometries of adsorbed species and identified transition states with the corresponding bond lengths. Atom colour legend: O (red), Zn (grey), H (light pink), C (brown). (For interpretation of the references to colour in this figure legend, the reader is referred to the Web version of this article.)

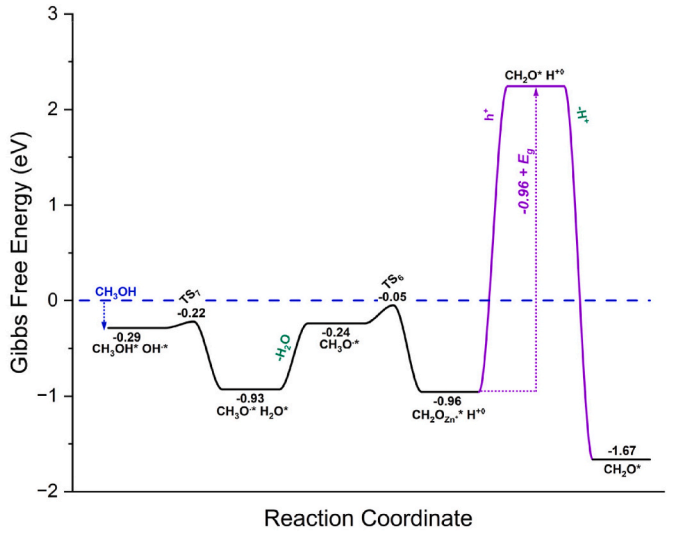

Fig. 14. Reaction coordinate diagram for the solvated oxidation of methanol to formaldehyde over the (100) wurtzite ZnO surface. Surface species bind to Zn_{3c}^{2+} sites, unless specified. Protons bind to O_{surf} sites. Notation is similar to Fig. 12, with the horizontal dashed line representing methanol.

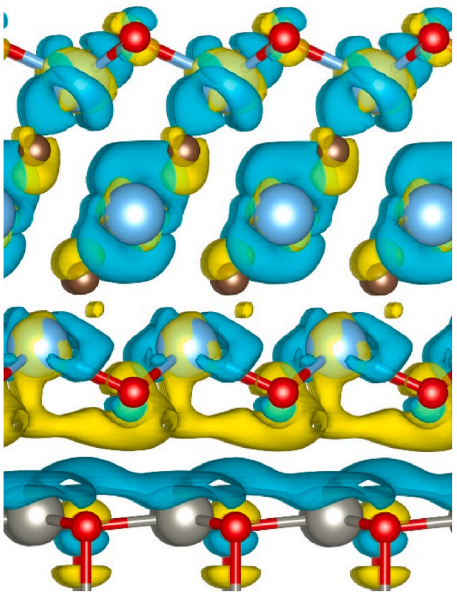

Fig. 15. Charge density distribution plots for the ZnO/MXene heterojunction. The regions show electron accumulation (yellow) and depletion (blue). (Isosurface value = 0.0013 $bohr^{-3}$). (For interpretation of the references to colour in this figure legend, the reader is referred to the Web version of this article.)

and O atoms. This configuration is stable and exhibits a substantial desorption barrier (0.52 eV), suggesting that formaldehyde is likely to undergo further surface reactions rather than desorb.

Alternatively, adsorbed methanol can interact with pre-adsorbed hydroxyl species on ZnO. In this case, the binding energy is slightly strengthened ($\Delta G = -0.29\,eV$), although no initial hydrogen bond forms between the two species. At the transition state, the methanol OH group forms a hydrogen bond with the surface OH• radical. This step proceeds with a low barrier of 0.07 eV and yields a methoxy radical and water, while the backward reaction faces a significantly higher barrier of 0.71 eV. The resulting methoxy radical then undergoes the same C–H bond scission as described in Fig. 14.

The mechanistic analysis presented in this work indicates that hydrogen production is primarily driven by sacrificial agent oxidation, facilitated by surface-bound hydroxyl radicals, following the pathways illustrated in Fig. 14. Compared to the hole-assisted sacrificial agent deprotonation pathway, the OH•-assisted oxidation is both more exergonic and kinetically favourable, and is therefore expected to dominate under aqueous conditions. The key role of OH• species in the photocatalytic hydrogen production process along with the synergistic interaction between methanol and water has been demonstrated also for TiO_2-based photocatalysts [18]. A schematic representation of the photocatalytic mechanism, highlighting the respective roles of ZnO and MXene in the hydrogen production process, is provided in Fig. S10.

3.5. Hydrogen formation

The elucidate the redox mechanism, the photocatalytic system was modelled by treating ZnO and MXene as distinct components with explicit structures. In this configuration, proton reduction and subsequent recombination of hydrogen radicals were proposed to occur on the MXene surface, which hosts the negative charge carriers, while ZnO accommodates the positive charge carriers. This is in line with other studies that have determined the transfer of electrons to the MXene component [47].This approach captures the charge separation at the ZnO/MXene heterojunction interface, as illustrated in the charge density distribution analysis reported in Fig. 15. Regions of electron accumulation are observed near the MXene surface (yellow), while electron depletion is localized on the ZnO surface (blue).

To explore the efficiency of Ti_3C_2 MXene towards photocatalytic hydrogen production, we investigated its ability to adsorb hydrogen across different surface coverages up to 1 ML (monolayer). It is worth noting that a high performing co-catalyst can not only facilitate electron transfer from the semiconductor but also catalyse the hydrogen evolution reaction (HER) effectively. According to the Sabatier principle, the optimal catalyst binds hydrogen with an adsorption free energy close to zero. Therefore, a hydrogen atom must not adsorb too strongly ($\Delta G_{ads} \ll 0$) or too weakly ($\Delta G_{ads} \gg 0$) to avoid either the poisoning of surface sites or lack of adsorption [48]. The bare Ti_3C_2 surface consists of Ti-backed (fcc) and C-backed (hcp) hollow sites. In isolated adsorption, the C-backed hollow site is more favourable ($\Delta G = -1.15\,eV$, Fig. S11a) over the Ti-backed site ($\Delta G = -0.86\,eV_2$ Fig. S11b). However, at higher coverages ($\geq$0.25 ML), optimized configurations favour hydrogen adsorption on the Ti-backed sites instead. While the average energy of adsorption gradually shifts towards 0 with increasing coverage, it remains moderately negative (−0.24 eV at 1 ML, Fig. 16a). This suggests that desorption of H_2 is kinetically hindered on the bare MXene, reducing its overall HER activity. However, the bare MXene surface is typically terminated with functional groups formed during etching and subsequent exposure to aqueous environments. Generally, a mix of functional groups would cover the surface [49], with the O-terminated $Ti_3C_2O_2$ configuration being the most stable and preferentially formed [50,51]. On this surface, hydrogen preferentially binds to O top sites (Fig. S12), forming terminal hydroxyl species. Adsorption on these sites is weaker ($\Delta G = -0.49\,eV$). As the coverage increases from 0.25 ML to 1 ML, the average adsorption energy approaches thermoneutrality at 0.75 ML and further adsorption becomes thermodynamically hindered (Fig. 16b). The resultant O-terminated structure indicates a more favourable balance between H adsorption and desorption, indicating enhanced HER activity compared to the bare MXene surface.

4. Conclusions

In this work, MXene-based heterostructures incorporating ZnO and CeO_2 were successfully synthesized using different preparation routes, and their photocatalytic performance toward hydrogen evolution was systematically investigated. The results demonstrate that the integration of Ti_3C_2Tx MXene significantly enhances photocatalytic activity by promoting efficient charge separation and facilitating interfacial

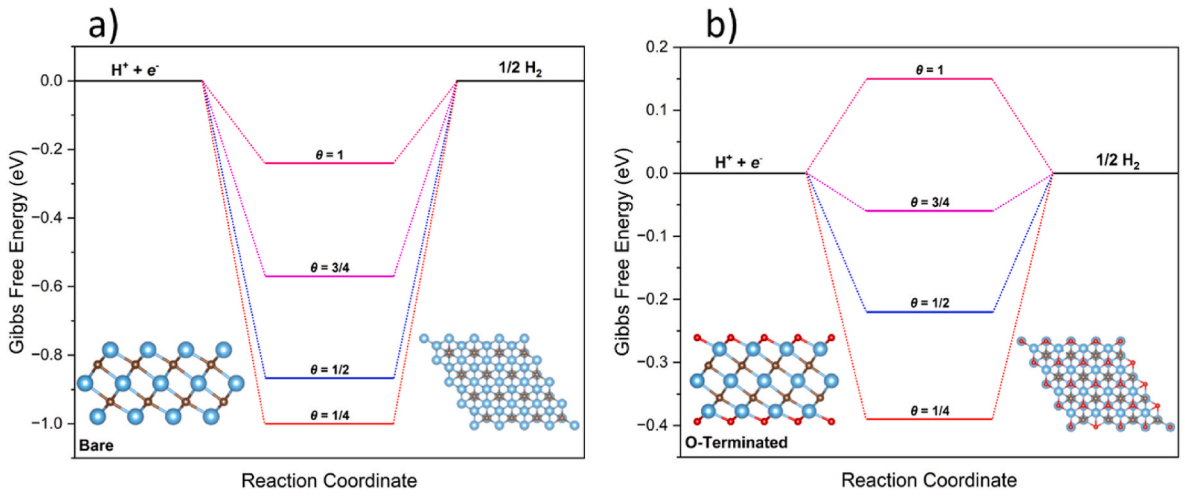

Fig. 16. Calculated free energy diagrams displaying the average adsorption free energy as a function of the coverage on a) bare and b) O-terminated MXene surfaces at 0.25, 0.50, 0.75, and 1.00 ML coverages.

electron transfer.

Among the investigated systems, the MXene_CeO_2_ZnO_H sample exhibited the highest hydrogen evolution rate, highlighting the beneficial synergistic effect of combining MXene with the CeO_2/ZnO heterojunction. The improved performance is attributed to the dual role of MXene as an electron mediator and of CeO_2 as a redox-active component through the reversible Ce^{4+}/Ce^{3+} couple, which together suppress charge recombination and enhance the availability of electrons for hydrogen production.

Mechanistic insights into water splitting revealed that the thermal dissociation step is facile, whereas the generation of hydroxyl radicals is limited by the photocatalytic process. In addition, the thermal decomposition of the model sacrificial agent proceeds readily with strong adsorption of the product onto the surface. Additionally, the O-terminated MXene surface exhibits the most favourable balance between hydrogen adsorption and desorption compared to the bare surface.

Structural and catalytic differences observed between the synthesis methods indicate that the preparation route plays a key role in determining the interfacial interaction between the components and, consequently, the photocatalytic efficiency. Although the materials exhibit relatively low specific surface areas, the results confirm that photocatalytic performance is primarily governed by electronic and interfacial properties rather than textural characteristics.

Overall, this study provides new insights into the role of MXenes in complex oxide heterostructures and demonstrates their potential as efficient electron mediators in photocatalytic hydrogen production systems. The findings contribute to the rational design of advanced photocatalysts for sustainable hydrogen generation. Future work will include systematic testing under standard sacrificial agents (e.g., methanol, triethanolamine) to enable direct benchmarking with literature.

CRediT authorship contribution statement

Paolo Iaconis: Writing – original draft, Methodology, Investigation, Formal analysis, Data curation. **Valeria Lagostina:** Writing – review & editing, Formal analysis, Data curation. **Francesco Ricco:** Investigation, Data curation. **Gabriele Enrico:** Investigation, Data curation. **Matthew J. Wigglesworth:** Writing – review & editing, Conceptualization. **Sergio Vernuccio:** Writing – review & editing, Supervision, Conceptualization. **Paola Calza:** Writing – review & editing, Supervision, Funding acquisition, Conceptualization. **Maria Cristina Paganini:** Writing – review & editing, Writing – original draft, Supervision, Methodology, Conceptualization.

Declaration of competing interest

The authors declare the following financial interests/personal relationships which may be considered as potential competing interests: Maria Cristina Paganini reports was provided by University of Turin Department of Chemistry. If there are other authors, they declare that they have no known competing financial interests or personal relationships that could have appeared to influence the work reported in this paper.

Acknowledgements

The authors would like to thank Dr Micaela Castellino (Politecnico di Torino) for the invaluable efforts in doing XPS measurements that improved the quality of our work and prof. Mattero Signorile for the fruitful discussion and for his help and supervision during the H_2 production experiments. This project has received funding from the European Union under the Horizon Europe Marie Skłodowska-Curie Actions (MSCA) Doctoral Network program (IN2AQUAS-grant agreement number 101119555); the authors acknowledge support from European Union- Next Generation EU, Mission 4 Component 1 CUP D53D23010160006 with MUR (Italy) through PRIN Project MAPEC (N.2022599 NR3) "Magnetic field assisted photo(electro) CO2 conversion – MAPEC and the Project CH4.0 under the MUR program "Dipartimenti di Eccellenza 2023–2027". SV acknowledges financial support from the rom the EPSRC/NERC-funded Great British Chemicals programme (UKRI2199) and from the Royal Academy of Engineering Industrial Fellowship (IF-2425-19-AI102).

Appendix A. Supplementary data

Supplementary data to this article can be found online at https://doi.org/10.1016/j.ijhydene.2026.155192.

References

[1] Ritchie H, Rosado P. Fossil fuels 2017. https://ourworldindata.org/fossil-fuels. [Accessed 27 November 2025].
[2] Liu J, Zhang S, Wang W, Zhang H. Photoelectrocatalytic principles for meaningfully studying photocatalyst properties and photocatalysis processes: from fundamental theory to environmental applications. J Energy Chem 2023;86:84–117. https://doi.org/10.1016/j.jechem.2023.06.038.
[3] Fujishima A, Honda K. Electrochemical photolysis of water at a semiconductor electrode. Nature 1972;238:37–8. https://doi.org/10.1038/238037a0.
[4] Gogotsi Y, Anasori B. The rise of MXenes. ACS Nano 2019;13:8491–4. https://doi.org/10.1021/acsnano.9b06394.

[5] Guo Z, Zhou J, Zhu L, Sun Z. MXene: a promising photocatalyst for water splitting. J Mater Chem A Mater 2016;4:11446–52. https://doi.org/10.1039/c6ta04414j.

[6] Yan T, Xu LC, Pan WG, Wang LW. MXene - a frontier exploiter in carbon dioxide conversion: synthesis and adsorption. Nano Today 2024;59. https://doi.org/10.1016/j.nantod.2024.102546.

[7] Cheng X, Zu L, Jiang Y, Shi D, Cai X, Ni Y, et al. A titanium-based photo-Fenton bifunctional catalyst of mp-MXene/TiO2-x nanodots for dramatic enhancement of catalytic efficiency in advanced oxidation processes. Chem Commun 2018;54:11622–5. https://doi.org/10.1039/c8cc05866k.

[8] Saini B, Harikrishna K, Laishram D, Krishnapriya R, Singhal R, Sharma RK. Role of ZnO in ZnO Nanoflake/Ti3C2MXene composites in photocatalytic and electrocatalytic hydrogen evolution. ACS Appl Nano Mater 2022;5:9319–33. https://doi.org/10.1021/acsanm.2c01639.

[9] Behera P, Ray A, Tripathy SP, Subudhi S, Acharya L, Biswal L, et al. Ti 3 C 2 MXene-Integrated MOF-derived C, N–ZnO@BCN nanocomposites for enhanced photocatalytic H 2 O 2 production and H 2 evolution. ACS Applied Engineering Materials 2025. https://doi.org/10.1021/acsaenm.5c00917.

[10] Shi K, Li X, Xiao Q, Wang Z, Yi W, Ren J, et al. Facile construction of ZnWO4/Ti3C2 MXene type-II heterojunctions via hydrothermal self-assembly: toward efficient clean energy conversion and environmental remediation. Fuel 2026;414:138332. https://doi.org/10.1016/j.fuel.2026.138332.

[11] Huang TY, Yang Z, Yang SY, Dai ZH, Liu YJ, Liao JH, et al. Construction of 2D/2D Ti3C2Tx MXene/CdS heterojunction with photothermal effect for efficient photocatalytic hydrogen production. J Mater Sci Technol 2024;171:1–9. https://doi.org/10.1016/j.jmst.2023.07.010.

[12] Chen F, Wu M, Xu Y, Zhang J, Luo J, Tian M. Construction of schottky-assisted Z-scheme heterojunction Cd0.3Zn0.7S@Ti3C2/Ag/CeO2 boosted carriers charge separation for efficient photocatalytic hydrogen production. Sep Purif Technol 2025;354. https://doi.org/10.1016/j.seppur.2024.128895.

[13] Tasqeeruddin S, Kanabar B, Ganesan S, Shankhyan A, Khatibi A, Tantawi D, et al. Next-generation MXene composites for clean hydrogen production: recent insights and innovations. J Mol Struct 2025;1346. https://doi.org/10.1016/j.molstruc.2025.143138.

[14] Yu C, Zhou W, Yu JC, Liu H, Wei L. Design and fabrication of heterojunction photocatalysts for energy conversion and pollutant degradation. Cuihua Xuebao/Chinese Journal of Catalysis 2014;35:1609–18. https://doi.org/10.1016/S1872-2067(14)60170-4.

[15] Cerrato E, Gionco C, Paganini MC, Giamello E, Albanese E, Pacchioni G. Origin of visible light photoactivity of the CeO2/ZnO heterojunction. ACS Appl Energy Mater 2018;1:4247–60. https://doi.org/10.1021/acsaem.8b00887.

[16] Brette F, Célérier S, Canaff C, Loupias L, Paris M, Habrioux A, et al. XPS binding energy shifts in 2D Ti3C2Tz MXene go largely beyond intuitive explanations: rationalization from DFT simulations and experiments. Small Methods 2025;9:2400848. https://doi.org/10.1002/smtd.202400848.

[17] Engelhard MH, Baer DR, Herrera-Gomez A, Sherwood PMA. Introductory guide to backgrounds in XPS spectra and their impact on determining peak intensities. J Vac Sci Technol A 2020;38:063203. https://doi.org/10.1116/6.0000359.

[18] Wigglesworth MJ, Ma R, Martsinovich N, Vernuccio S. Mechanistic insights into hydrogen evolution from methanol photoreforming on metal-loaded anatase: development of a microkinetic model. Chem Eng J 2025;523:168334. https://doi.org/10.1016/j.cej.2025.168334.

[19] Cai T, Wang L, Liu Y, Zhang S, Dong W, Chen H, et al. Ag3PO4/Ti3C2 MXene interface materials as a Schottky catalyst with enhanced photocatalytic activities and anti-photocorrosion performance. Appl Catal, B 2018;239:545–54. https://doi.org/10.1016/j.apcatb.2018.08.053.

[20] Wang H, Wu Y, Xiao T, Yuan X, Zeng G, Tu W, et al. Formation of quasi-core-shell In2S3/anatase TiO2@metallic Ti3C2Tx hybrids with favorable charge transfer channels for excellent visible-light-photocatalytic performance. Appl Catal, B 2018;233:213–25. https://doi.org/10.1016/j.apcatb.2018.04.012.

[21] Hieu VQ, Phung TK, Nguyen TQ, Khan A, Doan VD, Tran VA, et al. Photocatalytic degradation of methyl orange dye by Ti3C2–TiO2 heterojunction under solar light. Chemosphere 2021;276. https://doi.org/10.1016/j.chemosphere.2021.130154.

[22] Bechambi O, Jlaiel L, Najjar W, Sayadi S. Photocatalytic degradation of bisphenol A in the presence of Ce-ZnO: evolution of kinetics, toxicity and photodegradation mechanism. Mater Chem Phys 2016;173:95–105. https://doi.org/10.1016/j.matchemphys.2016.01.044.

[23] Tauc J. The optical properties of solids. New York: Academic Press; 1966.

[24] Mang A, Reimann K. Rübenacke St. Band gaps, crystal-field splitting, spin-orbit coupling, and exciton binding energies in ZnO under hydrostatic pressure. Solid State Commun 1995;94:251–4. https://doi.org/10.1016/0038-1098(95)00054-2.

[25] Ananda VR, Ramadhan FN, Kautsari AM, Amrillah T, Hermawan A, Yulizar Y, et al. Powder engineering of MXene-based heterojunction materials for photocatalysis and gas sensor applications. Adv Powder Technol 2025;36. https://doi.org/10.1016/j.apt.2025.104789.

[26] Eghbali P, Hassani A, Wacławek S, Andrew Lin KY, Sayyar Z, Ghanbari F. Recent advances in design and engineering of MXene-based catalysts for photocatalysis and persulfate-based advanced oxidation processes: a state-of-the-art review. Chem Eng J 2024;480. https://doi.org/10.1016/j.cej.2023.147920.

[27] Ta QTH, Sreedhar A, Tri NN, Noh JS. In situ growth of TiO2 on Ti3C2Tx MXene for improved gas-sensing performances. Ceram Int 2024;50:27227–36. https://doi.org/10.1016/j.ceramint.2024.05.020.

[28] Natu V, Benchakar M, Canaff C, Habrioux A, Célérier S, Barsoum MW. A critical analysis of the X-ray photoelectron spectra of Ti3C2Tz MXenes. Matter 2021;4:1224–51. https://doi.org/10.1016/j.matt.2021.01.015.

[29] Breaking the tribocorrosion threat_ an active-passive PANI microcapsules@MXene network enabling on-demand healing and lubrication in epoxy coatings [n.d].

[30] Henderson JD, Buchanan SDC, Grey LH, Biesinger MC. Zinc and cadmium: XPS chemical state determination and auger peak curve-fitting procedures. Appl Surf Sci 2026;730. https://doi.org/10.1016/j.apsusc.2026.166284.

[31] Duchoslav J, Steinberger R, Arndt M, Stifter D. XPS study of zinc hydroxide as a potential corrosion product of zinc: rapid X-ray induced conversion into zinc oxide. Corros Sci 2014;82:356–61. https://doi.org/10.1016/j.corsci.2014.01.037.

[32] Maslakov KI, Teterin YA, Popel AJ, Teterin AY, Ivanov KE, Kalmykov SN, et al. XPS study of ion irradiated and unirradiated CeO 2 bulk and thin film samples. Appl Surf Sci 2018;448:154–62. https://doi.org/10.1016/j.apsusc.2018.04.077.

[33] Vazirov RA, Sokovnin SY, Ilves VG, Bazhukova IN, Pizurova N, Kuznetsov MV. Physicochemical characterization and antioxidant properties of cerium oxide nanoparticles. J Phys Conf Ser 2018;1115. https://doi.org/10.1088/1742-6596/1115/3/032094. Institute of Physics Publishing.

[34] Su T, Hood ZD, Naguib M, Bai L, Luo S, Rouleau CM, et al. Monolayer Ti3C2 Tx as an effective Co-catalyst for enhanced photocatalytic hydrogen production over TiO2. ACS Appl Energy Mater 2019;2:4640–51. https://doi.org/10.1021/acsaem.8b02268.

[35] Zhu H, Fu X, Zhou Z. 3D/2D heterojunction of CeO2/Ultrathin MXene nanosheets for photocatalytic hydrogen production. ACS Omega 2022;7:21684–93. https://doi.org/10.1021/acsomega.2c01674.

[36] Zhan S, Yang Y, Taixu L, Sanja A, Lin W, Huilin H, et al. 0D/2D heterojunction photocatalysts for improved full-spectrum-light-driven hydrogen evolution. J Mater Chem A 2024;12:29278–87. https://doi.org/10.1039/D4TA06179A.

[37] Nemamcha HE, Vu NN, Tran DS, Boisvert C, Nguyen DD, Nguyen-Tri P. Recent progression in MXene-based catalysts for emerging photocatalytic applications of CO2 reduction and H2 production: a review. Sci Total Environ 2024;931. https://doi.org/10.1016/j.scitotenv.2024.172816.

[38] Ahmad I, Ahmed E, Ahmad M. The excellent photocatalytic performances of silver doped ZnO nanoparticles for hydrogen evolution. SN Appl Sci 2019;1. https://doi.org/10.1007/s42452-019-0331-9.

[39] Li H, Sun B, Gao T, Li H, Ren Y, Zhou G. Ti3C2 MXene co-catalyst assembled with mesoporous TiO2 for boosting photocatalytic activity of methyl orange degradation and hydrogen production. Chin J Catal 2022;43:461–71. https://doi.org/10.1016/S1872-2067(21)63915-3.

[40] Wang Z, Zhang Y, Chen Y, Wei P, Wang H, Yu H, et al. Surface -O terminated urchin-like TiO2/Ti3C2Ox (MXene) as high performance photocatalyst: interfacial engineering and mechanism insight. Appl Surf Sci 2023;615. https://doi.org/10.1016/j.apsusc.2023.156343.

[41] Shinagawa T, Takanabe K. Towards versatile and sustainable hydrogen production through electrocatalytic water splitting: electrolyte engineering. ChemSusChem 2017;10:1318–36. https://doi.org/10.1002/cssc.201601583.

[42] Sargeant E, Illas F, Rodríguez P, Calle-Vallejo F. Importance of the gas-phase error correction for O2 when using DFT to model the oxygen reduction and evolution reactions. J Electroanal Chem 2021;896. https://doi.org/10.1016/j.jelechem.2021.115178.

[43] Zou W, Dou K, Jiang Q, Xiang J, Kaun CC, Tang H. Nearly spherical CoP nanoparticle/carbon nanosheet hybrids: a high-performance trifunctional electrocatalyst for oxygen reduction and water splitting. RSC Adv 2019;9:39951–7. https://doi.org/10.1039/c9ra07334e.

[44] Dues C, Schmidt WG, Sanna S. Water splitting reaction at polar lithium niobate surfaces. ACS Omega 2019;4:3850–9. https://doi.org/10.1021/acsomega.8b03271.

[45] Yang Y, Liu J, Liu F, Wang Z, Wu D. FeS2-anchored transition metal single atoms for highly efficient overall water splitting: a DFT computational screening study. J Mater Chem A Mater 2021;9:2438–47. https://doi.org/10.1039/d0ta09903a.

[46] Janotti A, Van de Walle CG. Fundamentals of zinc oxide as a semiconductor. Rep Prog Phys 2009;72:126501. https://doi.org/10.1088/0034-4885/72/12/126501.

[47] Wei P, Chen Y, Zhou T, Wang Z, Zhang Y, Wang H, et al. Manipulation of charge-transfer kinetics via Ti3C2Tx (T = −O) quantum dot and N-Doped carbon dot coloading on CdS for photocatalytic hydrogen production. ACS Catal 2023;13:587–600. https://doi.org/10.1021/acscatal.2c04632.

[48] Hamdan S, Wigglesworth MJ, Muscetta M, Ma R, Helal MI, Martsinovich N, et al. Unravelling the photoactivity of metal-loaded TiO2 for hydrogen production: insights from a combined experimental and computational analysis. Int J Hydrogen Energy 2025;118:394–406. https://doi.org/10.1016/j.ijhydene.2025.03.184.

[49] Ibragimova R, Puska MJ, Komsa H-P. pH-Dependent distribution of functional groups on titanium-based MXenes. ACS Nano 2019;13:9171–81. https://doi.org/10.1021/acsnano.9b03511.

[50] Karlsson LH, Birch J, Halim J, Barsoum MW, Persson POÅ. Atomically resolved structural and chemical investigation of single MXene sheets. Nano Lett 2015;15:4955–60. https://doi.org/10.1021/acs.nanolett.5b00737.

[51] Xie Y, Naguib M, Mochalin VN, Barsoum MW, Gogotsi Y, Yu X, et al. Role of surface structure on Li-Ion energy storage capacity of two-dimensional transition-metal carbides. J Am Chem Soc 2014;136:6385–94. https://doi.org/10.1021/ja501520b.